



# Large Adaptive Optics Survey for Substellar Objects around Young, Nearby, Low-mass Stars with Robo-AO

Maïssa Salama<sup>1</sup> , James Ou<sup>1</sup> , Christoph Baranec<sup>1</sup> , Michael C. Liu<sup>2</sup> , Brendan P. Bowler<sup>3</sup> , Paul Barnes<sup>1</sup>, Morgan Bonnet<sup>2</sup>, Mark Chun<sup>1</sup> , Dmitry A. Duev<sup>4</sup> , Sean Goebel<sup>1</sup> , Don Hall<sup>1,7</sup>, Shane Jacobson<sup>1</sup>, Rebecca Jensen-Clem<sup>5</sup> , Nicholas M. Law<sup>6</sup> , Charles Lockhart<sup>1</sup>, Reed Riddle<sup>4</sup> , Heather Situ<sup>2</sup>, Eric Warmbier<sup>1</sup>, and Zhoujian Zhang<sup>2</sup>

<sup>1</sup>Institute for Astronomy, University of Hawai'i at Mānoa, Hilo, HI 96720, USA; [msalama@hawaii.edu](mailto:msalama@hawaii.edu)

<sup>2</sup>Institute for Astronomy, University of Hawai'i at Mānoa, Honolulu, HI 96822, USA

<sup>3</sup>Department of Astronomy, The University of Texas at Austin, Austin, TX 78712, USA

<sup>4</sup>Division of Physics, Mathematics, and Astronomy, California Institute of Technology, Pasadena, CA 91125, USA

<sup>5</sup>Astronomy & Astrophysics Department, University of California, Santa Cruz, CA 95064, USA

<sup>6</sup>Department of Physics and Astronomy, University of North Carolina at Chapel Hill, Chapel Hill, NC 27599-3255, USA

Received 2020 November 11; revised 2021 May 17; accepted 2021 May 19; published 2021 August 13

## Abstract

We present results from the Large Adaptive optics Survey for Substellar Objects, where the goal is to directly image new substellar companions ( $<70 M_{\text{Jup}}$ ) at wide orbital separations ( $\gtrsim 50$  au) around young ( $\lesssim 300$  Myr), nearby ( $<100$  pc), low-mass ( $\approx 0.1\text{--}0.8 M_{\odot}$ ) stars. We report on 427 young stars imaged in the visible ( $i'$ ) and near-infrared ( $J$  or  $H$ ) simultaneously with Robo-AO on the Kitt Peak 2.1 m telescope and later the Maunakea University of Hawaii 2.2 m telescope. To undertake the observations, we commissioned a new infrared camera for Robo-AO that uses a low-noise high-speed SAPHIRA avalanche photodiode detector. We detected 121 companion candidates around 111 stars, of which 62 companions are physically associated based on Gaia DR2 parallaxes and proper motions, another 45 require follow-up observations to confirm physical association, and 14 are background objects. The companion separations range from 2 to 1101 au and reach contrast ratios of 7.7 mag in the near-infrared compared to the primary. The majority of confirmed and pending candidates are stellar companions, with  $\sim 5$  being potentially substellar and requiring follow-up observations for confirmation. We also detected a  $43 \pm 9 M_{\text{Jup}}$  and an  $81 \pm 5 M_{\text{Jup}}$  companion that were previously reported. We found 34 of our targets have acceleration measurements detected using Hipparcos–Gaia proper motions. Of those,  $58^{+12}_{-14}\%$  of the 12 stars with imaged companion candidates have significant accelerations ( $\chi^2 > 11.8$ ), while only  $23^{+11}_{-6}\%$  of the remaining 22 stars with no detected companion have significant accelerations. The significance of the acceleration decreases with increasing companion separation. These young accelerating low-mass stars with companions will eventually yield dynamical masses with future orbit monitoring.

*Unified Astronomy Thesaurus concepts:* [Low mass stars \(2050\)](#); [Binary stars \(154\)](#); [Brown dwarfs \(185\)](#); [Surveys \(1671\)](#); [Optical observation \(1169\)](#); [Infrared astronomy \(786\)](#); [Astronomical instrumentation \(799\)](#)

*Supporting material:* machine-readable tables

## 1. Introduction

Over the past three decades, our knowledge of planetary systems has expanded from just our solar system to a multitude of planetary architectures. The Kepler mission detected thousands of exoplanets in close-in orbits ( $\lesssim 1$  au) as they transit their host star. The radial velocity method has been used to discover thousands of exoplanets out to slightly farther orbits ( $\lesssim 5$  au). Direct imaging helped identify a complementary population of substellar companions ( $2\text{--}75 M_{\text{Jup}}$ ), namely planets and brown dwarfs, at large projected separations ( $\sim 5\text{--}8000$  au). The existence of these companions at wide separations has played a critical role in shaping theories about the formation and migration of brown dwarfs and planets, through the development of mechanisms such as core/pebble accretion (Lambrechts & Johansen 2012), disk instability (Durisen et al. 2007; Kratter & Lodato 2016), cloud fragmentation (Bate et al. 2003), and dynamical scattering (Veras et al. 2009) on various timescales and orbital separations. These mechanisms predict correlations between the presence of a wide-orbit companion and certain environmental characteristics, such as the presence or absence of other companions, circumstellar disk

morphologies, and the eccentricity of the companion's orbit, which can be compared to observational studies. The IAU currently defines the boundary between brown dwarfs and planets at  $13 M_{\text{Jup}}$ , but it remains unresolved whether this is an artificial boundary or reflective of a natural division that links observational properties of these objects to dominant formation mechanisms (Chabrier et al. 2014; Schlaufman 2018).

Population demographic studies are necessary to search for trends in the orbital architectures, primary and companion masses, ages, and environments of systems with wide-orbit substellar companions and to clarify the boundary between brown dwarfs and massive exoplanets. However, the number of discoveries so far has limited the statistical analysis of these trends. Large exoplanet imaging searches, each on the order of hundreds of targets, have discovered between 0 and 4 substellar companions, bringing the total detections to  $<20$  objects in the planetary-mass regime ( $\lesssim 13 M_{\text{Jup}}$ ) and another  $\sim 100$  in the brown dwarf regime (Deacon et al. 2014; Bowler 2016; Bowler & Nielsen 2018; Baron et al. 2019). Bowler et al. (2020) conducted one of the first population demographic studies comparing the eccentricity distributions of substellar companion orbits over various parameters (e.g., mass, separation, and age). With a sample size of 27 substellar companions with

<sup>7</sup> Author is deceased.

orbital measurements, they found differences in the peaks of the distributions but could not constrain the exact shape of the distributions. Population studies with larger sample sizes are needed to better understand how these substellar objects form and evolve, as well as determine the natural boundary distinguishing brown dwarfs from massive exoplanets. A key step is to conduct a survey large enough to greatly boost the detections of these rare objects. This will allow us to perform more detailed population studies to test formation and evolution models.

Many of the early direct imaging surveys focused on massive stars because of the better adaptive-optics (AO)-corrected image quality and easier identification of young stars. However, low-mass stars are by far the most abundant stars in the galaxy, comprising roughly 75% of all stars (Bochanski et al. 2010). Several direct imaging surveys focusing on low-mass stars have now been conducted. For example, the Planets Around Low-Mass Stars (PALMS; Bowler et al. 2015a) survey observed 122 young M dwarfs with Keck/NIRC2 and Subaru/HiCIAO and detected 4 brown dwarf companions and no planetary companions. The M-dwarf Statistical Survey for direct Imaging of massive Exoplanets (MASSIVE; Lannier et al. 2016) observed 58 young and nearby M dwarfs and did not detect new substellar companions. The Planet Search around Young-associations M dwarfs (PSYM-WIDE; Naud et al. 2017), a deep seeing-limited survey, observed 95 stars with Gemini/GMOS and discovered one planetary companion.

Most stars are believed to have formed as part of a multiple system from the collapse and fragmentation of cloud cores (Larson 2002). However, the frequency of multiple systems has been observed to decrease with age (Duchêne & Kraus 2013), implying that as a stellar system evolves, dynamical interactions cause the ejection of companions (Reipurth et al. 2014). Thus, multiplicity statistics of young stars are useful for placing boundary conditions in evolutionary models exploring companion loss processes.

AO technology, which corrects for the blurring effect of the atmosphere, has enabled the discovery of many wide-orbit substellar companions by direct imaging. We are conducting a companion survey using Robo-AO, a robotic laser AO instrument (Baranec et al. 2014) at the Kitt Peak 2.1 m and Maunakea UH 2.2 m telescopes. Robo-AO's infrared science camera is equipped with a SAPHIRA (Selex Avalanche Photodiode for High-speed Infrared Array) detector (Baranec et al. 2015). This is a new type of infrared detector using electron-avalanche mechanisms to boost the signal while keeping the read noise fixed. As such, our survey is also testing the sensitivity and on-sky performance of these detectors.

We report here on the results from our observations as part of the Large Adaptive optics Survey for Substellar Objects (LASSO). The goal of LASSO is to search for wide-orbit (50–1500 au), substellar companions around young ( $\lesssim 300$  Myr), nearby ( $< 100$  pc), low-mass ( $0.1\text{--}0.8 M_{\odot}$ ) stars. In Section 2 we introduce the LASSO survey, target selection (Section 2.1), Robo-AO instrument (Section 2.2), observations (Section 2.3), data reduction (Section 2.4), and companion detection method (Section 2.5). In Section 3 we report the results of our observations, physical association determination (Section 3.1), and optical–infrared colors (Section 3.2). In Section 4 we discuss and analyze triple systems (Section 4.1), accelerating stars (Section 4.2), substellar objects (Section 4.3), and survey

yields and expectations (Section 4.4), and in Section 5 we summarize our main conclusions.

## 2. Survey and Observations

The objective of LASSO is to find new substellar companions at wide separations in order to carry out population studies of these rare objects. We surveyed young, nearby, low-mass stars because substellar objects are brighter when they are younger; it is easier to resolve objects at small physical separations when they are closer to us, and we are more sensitive to lower-mass companions in systems with lower-mass primaries. This is an ongoing survey with more observations to come from a prioritized sample.

### 2.1. LASSO Target Selection

We used the Cool Dwarf Catalog (CDC; Muirhead et al. 2018) as our starting sample. Its purpose is to identify cool dwarf targets for the Transiting Exoplanet Survey Satellite (TESS). Because young low-mass stars have chromospheric activity due to strong magnetic dynamos caused by their deep convective envelopes and differential rotation, they can be identified by excesses in the UV. In order to select for young stars, we cross-matched the CDC with the Galaxy Evolution Explorer (GALEX; Martin et al. 2005; Morrissey et al. 2007). Following Rodriguez et al. (2013), we applied the following selection criteria:

$$\text{NUV} - W1 \leq 12.5 \text{ mag} \quad (1)$$

$$J - W2 \geq 0.8 \text{ mag} \quad (2)$$

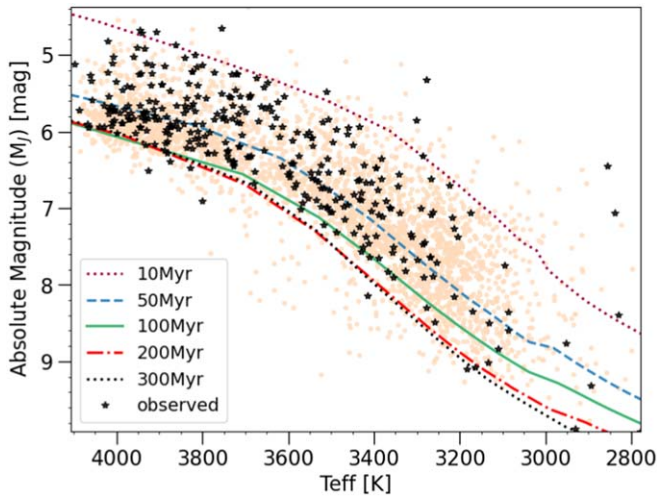
$$\text{NUV} - W1 < 7 \times (J - W2) + 5.5 \text{ mag}, \quad (3)$$

where NUV photometry is from GALEX,  $J$  magnitudes are from the Two Micron All Sky Survey (2MASS; Skrutskie et al. 2006), and  $W1$  ( $3.4 \mu\text{m}$ ) and  $W2$  ( $4.6 \mu\text{m}$ ) are from the Wide-field Infrared Survey Explorer (WISE; Wright et al. 2010). The remaining targets were then cross-matched with Gaia DR2 (Gaia Collaboration et al. 2016, 2018) to filter by measured proper motion and distance. Only targets within 100 pc were selected. Finally, we selected only targets observable from Kitt Peak (KP), and later Maunakea (MK), by limiting to targets with decl.  $> -30^{\circ}$  and  $-35^{\circ}$ , respectively. Targets with  $i' \leq 15$  mag were selected, or  $V \leq 17$  mag when no  $i'$ -band measurement was available in the CDC.

The resulting target list comprises 2787 stars for Kitt Peak and 3291 stars for Maunakea. Properties of our sample are shown in Figure 1, with evolutionary isochrones overlaid. Most targets are estimated to be between  $\sim 10$  and 300 Myr old, though no detailed independent age estimates were performed and some targets may be older than expected (see discussion in Section 4.4). The targets are predominantly M dwarfs with some late-K-type stars. They span temperatures of  $\sim 3000\text{--}4000$  K, and masses of  $\sim 0.1\text{--}0.8 M_{\odot}$ . We report Robo-AO imaging of 321 stars from this sample in this paper. The observed stars were selected by the Robo-AO queue system (Section 2.2).

#### 2.1.1. Sco-Cen Targets

In order to compare a younger sample of targets to our young field sample, after moving Robo-AO to Maunakea in 2019 we added targets from the Scorpius-Centaurus (Sco-Cen) association, which is the youngest and nearest OB association observable from the northern hemisphere (de Zeeuw et al. 1999; Wright & Mamajek 2018). The Sco-Cen association is farther than our



**Figure 1.** LASSO young field target sample (light orange dots) with isochrones from the Baraffe et al. (2015) evolutionary models overlaid. The effective temperatures and  $J$ -band magnitudes are from the CDC, and Gaia DR2 was used to determine  $J$ -band absolute magnitudes. The estimated age range of our target sample is  $\sim 10$ –300 Myr. Observed stars reported in this paper are shown as black stars.

young field sample, at an average distance of 140 pc, but it is younger, with an estimated age range of 5–15 Myr. We will thus be more sensitive to lower-mass objects than our field sample, but at slightly larger orbital separations. We used the Villa Vález et al. (2018) sample that isolated the pre-main-sequence population of stars in the Sco-Cen association using Gaia DR2 and applied the same color selection criteria as used by the CDC to select low-mass cool stars:

$$V - J > 2.7 \text{ mag} \quad (4)$$

$$M_V > 2.2 \times (V - J) - 2.0 \text{ mag.} \quad (5)$$

We also applied the same decl. and magnitude cuts (decl.  $> -35^\circ$  and  $i' \leq 15$  mag) as for our field sample. This additional sample consists of 668 targets,  $\sim 60\%$  of which are in the Upper Scorpius region, the youngest (5–15 Myr) subgroup of the association. We report Robo-AO imaging for 24 stars from this sample in this paper.

### 2.1.2. Pre-LASSO Targets

Before we finalized the target list above, and prior to the CDC and Gaia data releases, we used a preliminary target list of young active M dwarfs. These targets were selected from the cross-match of color-selected samples from Frith et al. (2013) and Haakonsen & Rutledge (2009), described in Bowler et al. (2019). In this paper we also report on Robo-AO imaging of 82 stars selected from this preliminary target list, which would not have been part of our LASSO list for the following reasons: 19 were not part of the CDC, 42 did not yield a match in GALEX, and 21 did not satisfy the selection criteria described in Equations (1)–(3). Thirty-one additional stars were also selected and observed from this preliminary target list, but would have been part of our LASSO sample and thus were included in our LASSO count discussed in Section 2.1.

Table 1 summarizes the number of stars reported in this paper and which list they come from.

**Table 1**  
Observed Stars Target Lists

Target List	Number of Stars Observed
LASSO young field late-K/M dwarfs	321
Pre-LASSO young field M dwarfs	82
Sco-Cen association late-K/M dwarfs	24
Total	427

## 2.2. Robo-AO Instrument

We conducted the observations with the Robo-AO instrument first at the Kitt Peak National Observatory 2.1 m telescope in Arizona, and later at the UH 2.2 m telescope on Maunakea, Hawai‘i (Baranec et al. 2014; Salama et al. 2016; Jensen-Clem et al. 2018; Salama et al. 2018). Robo-AO is equipped with both visible and infrared science cameras with a dichroic mirror simultaneously sending wavelengths shorter than  $\lambda = 950$  nm to the visible camera and the longer wavelengths to the infrared camera. Robo-AO uses a Rayleigh-scattering laser guide star with a line-of-sight focus at  $\sim 10$  km. The AO system runs at a rate of 1.2 kHz to correct high-order wave-front aberrations. In order to correct the tip-tilt motion of the star (not sensed by the laser guide star), we process the images with post facto shift-and-add, with data taken at 20 Hz in the infrared and 8.6 Hz in the visible. See Jensen-Clem et al. (2018) for more details.

We installed Robo-AO on the 2.1 m telescope on Kitt Peak, Arizona, from 2015 November to 2018 June. We conducted our observations after commissioning the infrared camera in 2016 November and while we were still testing and characterizing the performance of the detector and integrating the readout software within our automated observing routines. Each observation consists of a 5 minute exposure with 1–2 minutes of overhead due to telescope slewing and pointing, and laser guide star acquisition. The Robo-AO intelligent observing queue is described in Riddle et al. (2014).

### 2.2.1. Infrared Camera

In order to extend the scope of observable objects to much cooler and lower-mass objects (brown dwarfs and massive exoplanets) we added an infrared science camera with a SAPHIRA detector (Salama et al. 2018). Selex Avalanche Photodiode for HgCdTe InfraRed Array (SAPHIRA) detectors (Finger et al. 2014) provide photon-counting technology at infrared wavelengths (Atkinson et al. 2018). SAPHIRA detectors make use of electron-avalanche mechanisms within each pixel to effectively multiply the signal without increasing the read noise and thus improving the signal-to-noise ratio (S/N). SAPHIRA detectors allow for almost noiseless signal amplification and ultralow dark currents (Atkinson et al. 2017), which is especially beneficial for ground-based astronomical observations of photon-starved targets (e.g., Goebel et al. 2018; Bond et al. 2020; Hippler et al. 2020). This type of high-speed detector is particularly useful to minimize the degrading effect of the tip-tilt displacement on image quality by taking multiple short-exposure images while adding negligible noise (Jensen-Clem et al. 2018).

The infrared camera filter is located inside of the camera dewar and maintained at a temperature of 85 K. After testing different filters in the lab, calculating sensitivity limits, and

**Table 2**  
Robo-AO Science Cameras

	Visible Camera	Infrared Camera
Detector	EMCCD	SAPHIRA
Wavelengths	400–950 nm	0.8–2.5 $\mu\text{m}$
Format	1024 $\times$ 1024 pixels	320 $\times$ 256 pixels
Pixel size	13 $\mu\text{m}$	24 $\mu\text{m}$
Field of view	36" $\times$ 36" (KP) 26" $\times$ 26" (MK)	20".5 $\times$ 16".5 (KP) 14".5 $\times$ 11".5 (MK)
Plate scale	35 mas/pixel (KP) 25 mas/pixel (MK)	64 mas/pixel (KP) 46 mas/pixel (MK)
Filters	$i'$	$J$ (KP), $H$ (MK)
Sampling rate	8.6 Hz	20 Hz

changing the filter on sky at Kitt Peak, we determined that we were most sensitive to substellar objects in the  $J$  band due to the high thermal background at longer wavelengths. Substellar objects are brighter in the  $H$  band, and because the thermal background is lower due to the colder temperatures on Maunakea, we installed an  $H$ -band filter when we moved to the UH 2.2 m telescope.

### 2.2.2. Visible Camera

Robo-AO also has an EMCCD visible-light science camera with a filter wheel. The filter wheel includes the  $g'$ ,  $r'$ ,  $i'$ , and  $z'$  filters as well as a long-pass “lp600” filter, allowing wavelengths longer than 600 nm through. We carried out our observations in the  $i'$  band for optimal image sharpness. The characteristics of both science cameras are summarized in Table 2.

### 2.3. Observations

We observed a total of 427 stars with Robo-AO. 346 observations were carried out on the 2.1 m telescope on Kitt Peak, Arizona from 2017 to 2018 June. Ninety-eight observations were conducted in 2019 May and October on the UH 2.2 m telescope on Maunakea, 17 of which we had also previously observed at Kitt Peak. We obtained simultaneous images in the  $i'$  band and  $J$  band (on Kitt Peak) or  $i'$  band and  $H$  band (on Maunakea) for 432 of our observations. We did not capture simultaneous visible images for 12 stars, as the infrared camera software was not yet fully integrated with the Robo-AO system. The median measured seeing in the  $i'$  band was  $1''.53 \pm 0''.26$  and  $0''.97 \pm 0''.24$  at Kitt Peak and Maunakea, respectively. Table 11 in the Appendix lists all of the observed targets along with the observing conditions and achieved contrasts.

### 2.4. Data Reduction

#### 2.4.1. Infrared Camera

The SAPHIRA camera produces raw data cubes containing the sequences of frames resulting from nondestructive readouts. We first subtract each frame from the subsequent frame to produce a differential frame, which is inherently bias corrected. To calibrate these differential frames we then subtract the sky background and divide by the flat-field response. For the Robo-AO observations at the UH 2.2 m telescope, an IR source to produce flat fields had not yet been installed. Instead, we derived the per-pixel response from sky background images taken over the course of the observing program. Assuming

linear response, the signal  $s(t)$  returned by a pixel is the result of its response  $r$ , source flux over time  $f_{\text{source}} \times t$ , dark current (fixed pattern noise) over time  $d \times t$ , and bias  $b$ :

$$s(t) = r \times f_{\text{source}} \times t + d \times t + b. \quad (6)$$

With fixed integration time, bias correction through differential frames, and using the median of each background as the source flux, the normalized response for each pixel can be estimated through linear regression. For consistency, we also used this process for the Kitt Peak observations. We identified pixels with poor response by sigma clipping reduced background images and replaced these pixel values by Gaussian interpolation of surrounding pixels. This affected  $\sim 2.3\%$  of pixels at Kitt Peak and  $\sim 1\%$  of pixels at Maunakea. This improvement is likely due to readout electronic hardware modifications implemented while moving Robo-AO from Kitt Peak to Maunakea.

In the Kitt Peak observations we found linear artifacts that survived background subtraction and flat-fielding. These manifested as horizontal lines 32 pixels in length that appeared in random rows and were offset from the pixels in the rows above or below. Their locations corresponded to detector readout electronics and were not found in Maunakea observations. We suspect there may have been camera readout effects dependent on either hardware calibration or operating temperature, which improved after the hardware modifications and move to Maunakea. We mitigated these by subtracting a 10% quantile value from each 32 pixel-long row segment corresponding to the readout electronics (higher quantiles over-subtracted where stars or companions were present).

Tip-tilt motion is not sensed by the laser guide star system and is handled post facto by a modified shift-and-add routine. We stack the calibrated differential frames using the centroid position of the brightest star. This is performed with subpixel precision by weighting flux contributions from each pixel in subsequent frames by their proportional overlap over the output pixels, similar to the Drizzle algorithm (Fruchter & Hook 2002) but without shrinking the input pixels. We also produced images using shift-and-median instead of shift-and-add, which helped suppress noise artifacts not already removed by the calibrations. We selected the shift-and-median reduced image instead of the shift-and-add result for  $\sim 60\%$  of our observations.

Additionally, we developed an optional adaptation of the GenSTAC technique (Howard et al. 2018) to handle low-S/N frames, where target identification and centroid positioning can be unreliable in individual frames. A series of low-S/N frames are stacked together until the S/N is comparable to surrounding higher quality frames. The resulting centroid is then assigned to the center frame of the stack. The positioning for all other low-S/N frames in the stack is estimated by cubic spline interpolation of the centroid positions of the surrounding stack center frames and higher quality frames. Reduced images from this technique were selected for  $\sim 10\%$  of our observations and denoted in our list of observations (see Appendix, Table 11).

#### 2.4.2. Visible Camera

For each raw image frame, we subtract the background and apply a flat-field correction. We then process them through the image registration pipeline (first, the “bright-star” pipeline), which stacks the individual short-exposure frames on the brightest star in the field, to correct for the tip-tilt motion not

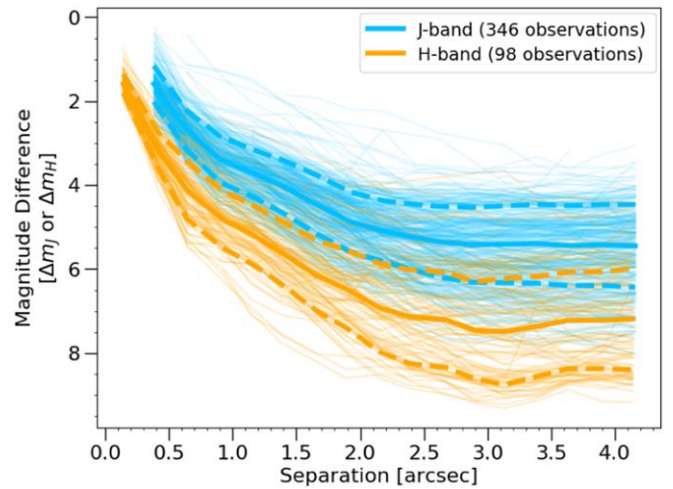
sensed by the laser guide star system. However, if the registration pipeline produces an FWHM  $< \lambda/D$ , then it is considered a failed registration, meaning it stacked on a bright pixel because the target was too faint. We then reprocess these images through the “faint-star” pipeline, which stacks all the frames, to create a reference frame, which is dark and flat corrected, then high-pass filtered and centered on the guide star. Each individual raw frame is then also dark and flat corrected, high-pass filtered, windowed, and finally registered to the reference frame. We also process the images through the high-contrast pipeline, in order to maximize the sensitivity to detect faint companions. This pipeline consists of applying a high-pass filter to remove light from the stellar halo, then a synthetic PSF of the star is generated by the Karhunen-Loève Image Processing (KLIP) algorithm, which makes use of a PSF reference library of Robo-AO observations and is subtracted from the observed PSF. A detailed description and performance analysis of the data reduction pipelines for the visible camera are available in Section 3 of Jensen-Clem et al. (2018).

## 2.5. Companion Detection

### 2.5.1. Infrared Camera

For each reduced image, we generated a radial average and subtracted it from the original to remove most of the primary starlight. We then visually inspected the radially subtracted images to flag companion candidates. Next, we calculated the centroid location of the star and any companion candidates. We then measured the S/N of the companion candidate by calculating the flux of the companion candidate in a circular aperture, subtracting from it the median background flux in an annulus around the star at the same separation as the companion candidate (while masking the companion candidate itself), and dividing by the noise in that same annulus. We did this over a range of aperture radii and calculated the companion candidate flux ratio with the primary star using the aperture size corresponding to the highest S/N. In combination with visual vetting of detections in our images, we applied an  $S/N > 5$  threshold (in at least either the visible or infrared image) to report a detection as a companion candidate. The errors were calculated from the standard deviation of the measurements on the individual (prestacked) observations and combined with the 5 mas positional systematic uncertainty after correcting for distortion, as reported in Jensen-Clem et al. (2018). The average measurement uncertainties are  $0''.03$  in separation,  $1''.5$  in PA,  $0.08$  mag in  $i'$ -band contrast,  $0.12$  mag in  $J$ -band contrast, and  $0.20$  mag in  $H$ -band contrast.

The sensitivity of our observations was determined through the injection and recovery of fake companions in the images. For each observation, we scaled a copy of the target star to a given contrast, then injected that scaled PSF at a given separation and position angle in the image. We then subtracted the radial average of the injected image. We did this for a range of separations, position angles, and contrasts and then determined the contrast at each position where the injected companion could no longer be recovered, using an S/N threshold of 5. At each separation, we adopted the median achieved contrast over the range of position angles to generate an individual contrast curve for each target (Figure 2). For stars with companion candidates, we masked the companion when generating the contrast curve.

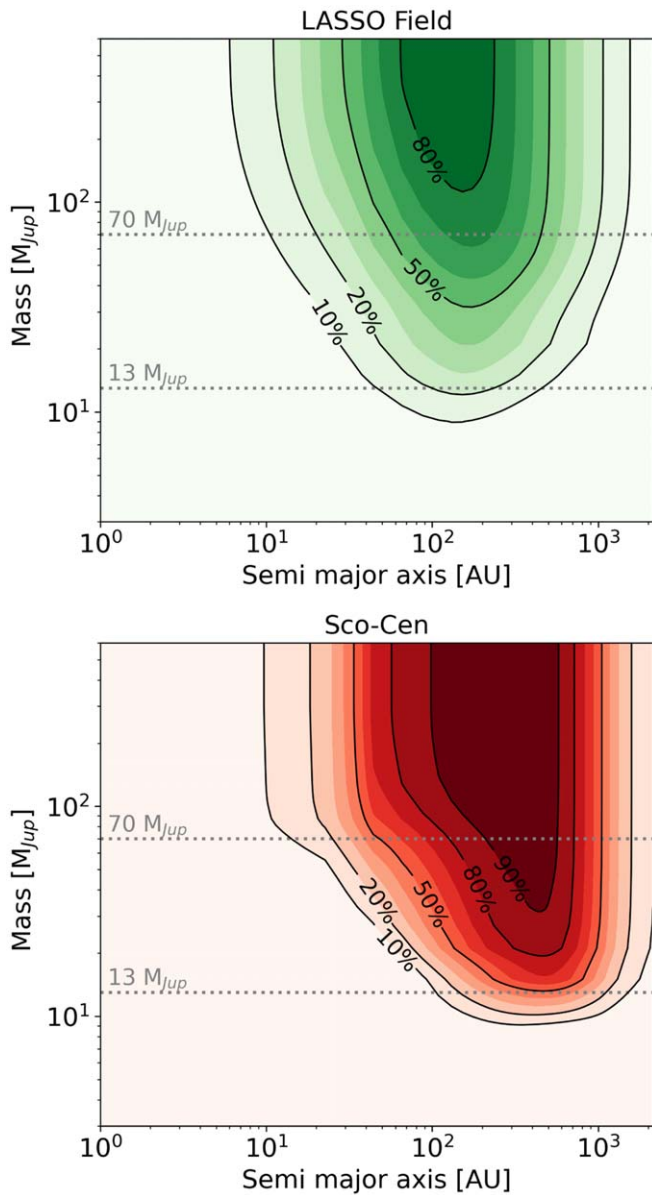


**Figure 2.** Contrast curves from LASSO Robo-AO observations in the  $J$  band on the 2.1 m telescope on Kitt Peak, Arizona (blue), and in the  $H$  band on the 2.2 m UH telescope on Maunakea, Hawai‘i (orange). The solid line is the median contrast curve and the dashed lines are  $\pm 1$  standard deviation.

In order to convert our contrast curves to detection sensitivity of companion mass and physical separation, we need to take into account the distance to each primary star, its magnitude, and evolutionary models to compute companion masses. Using each observed target’s Gaia DR2 parallax, we converted the contrast curve of magnitude differences to companion absolute magnitudes as a function of projected physical separation in astronomical units. From the absolute magnitudes and using evolutionary models from Chabrier et al. (2000) and Baraffe et al. (2015), we estimated a range of 100 companion masses corresponding to a range of 100 ages from 10 to 300 Myr sampled uniformly in log-space for young field targets, and 30 ages from 5 to 15 Myr sampled uniformly in log-space for Sco-Cen targets. We then used the python package `EXODMC` (Bonavita 2020) to generate a detection sensitivity map for each sampled age for each target. `EXODMC` is a Monte Carlo simulation code, which generates a synthetic population of 1000 planets with a range of orbital parameters. The assumptions and models used to generate this population are explained in Bonavita et al. (2012). We combined the detection sensitivity maps generated for each star at each age to estimate our overall detection sensitivity for young field stars (this includes both the LASSO and pre-LASSO stars, as their sensitivity maps were nearly identical) and Sco-Cen association stars, shown in Figure 3 and summarized in Table 3.

### 2.5.2. Visible Camera

The Robo-AO automated data reduction pipeline for the visible camera produces PSF-subtracted images and contrast curves for each observation. We visually inspected the images to flag companion candidates. Companion candidate measurements and S/N values were calculated in the same way as described for the infrared camera above. We used the contrast curves generated by the high-contrast pipeline for each observation to determine the sensitivity of our survey in the visible. Details about the performance and achievable contrasts of Robo-AO in the visible can be found in Figure 13 of Jensen-Clem et al. (2018).



**Figure 3.** Detection sensitivity for young field targets (top) and Sco-Cen targets (bottom). The contrast curves for each star were converted to physical separation in astronomical units using the Gaia DR2 distance, and the contrast was converted to companion mass using isochrone models over a range of ages (10–300 Myr for field stars and 5–15 Myr for Sco-Cen stars). The completeness was then determined using the EXODMC synthetic population simulation code.

**Table 3**  
Robo-AO Survey Detection Sensitivity

Companion Mass	Detection Probability		
	10%	50%	90%
LASSO field stars			
70 $M_{Jup}$	10–1425 au	50–450 au	...
40 $M_{Jup}$	15–1100 au	95–300 au	...
13 $M_{Jup}$	45–440 au	...	...
Sco-Cen association stars			
70 $M_{Jup}$	15–2000 au	45–1050 au	210–570 au
40 $M_{Jup}$	30–2000 au	80–1045 au	330–525 au
13 $M_{Jup}$	105–1525 au	450–500 au	...

### 2.5.3. False Triples

For some bright companions, the frame stacking may lock onto the centroid of the companion instead of the primary in some of the frames. This produces a “false triple” image where the companion appears on both sides of the primary, at the same separation and  $180^\circ$  rotated. We measured the contrast for both locations of the companion, masking both companion locations when measuring the background and noise in the annulus around the star. We then combined the measurements following Law (2006) to get the final contrast. This effect can be seen in both the visible and infrared data pipelines. We corrected four of our companion candidate contrast measurements for this effect.

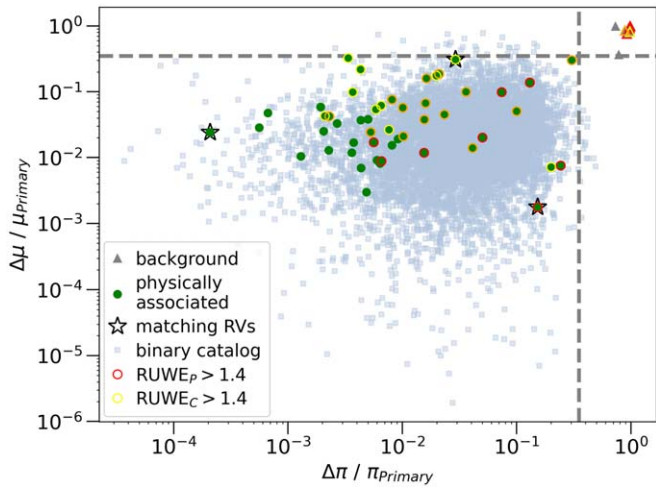
## 3. Results

We detected a total of 121 companion candidates near 111 stars using the Robo-AO infrared camera: 100 in the  $J$  band at Kitt Peak and 25 in the  $H$  band at Maunakea (including 4 observed and detected at both telescopes). We acquired simultaneous images with the visible camera of 107 stars with 118 companion candidates and detected 100 of these companion candidates in the  $i'$  band. The resulting detection measurements are summarized in Table 6 in the Appendix.

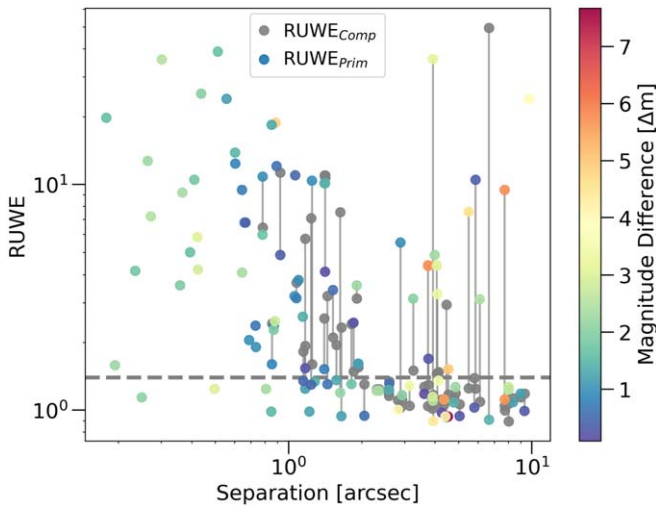
### 3.1. Physical Association

We searched Gaia DR2 for objects at the same location as our companion candidates and found matches for 75 of them. Of those, 62 had parallax and proper motion measurements. To estimate the possible physical association of the companion candidate and primary star, we compared their parallaxes and proper motions. We calculated the ratios of the primary – companion difference in parallax ( $\Delta\pi$ ) to the parallax of the primary ( $\pi_{\text{Primary}}$ ) and the primary – companion difference in proper motion ( $\Delta\mu$ ) to the proper motion of the primary ( $\mu_{\text{Primary}}$ ). In order to establish reasonable thresholds on these ratios, we compared our sample of primary – companion pairs to the Gaia DR2 selected wide comoving binaries from Jiménez-Esteban et al. (2019), shown in Figure 4. Jiménez-Esteban et al. (2019) determine pairs to be comoving if their differences in parallax and proper motions in R.A. and decl. are less than  $2\sigma$ , where  $\sigma$  is the maximum error of the two measurements. However, we opted to not directly include the errors in our thresholds because the majority of our candidates have large ( $>1.4$ ) renormalized unit weight error (RUWE) values, which indicates an issue with the astrometry solution, which uses a single star model. Such a large RUWE could indicate the Gaia DR2 measurements are affected by the presence of the companions. Jiménez-Esteban et al. (2019) only included sources with  $\text{RUWE} < 1.4$  and made further sample restrictions to ensure reliable error estimates. Figure 5 shows RUWE values for our sample as a function of separation. Stars with closer companions have large RUWEs, which suggests that the large RUWE is due to the presence of a companion. Therefore, we have determined objects with  $\Delta\pi/\pi_{\text{Primary}}$  or  $\Delta\mu/\mu_{\text{Primary}} > 0.35$  to very likely be background objects.

Twelve objects clearly stand out as background objects, while the other 50 companions all appear to be consistent with physical association. In addition, three of our pairs have Gaia DR2 radial velocity (RV) measurements for both components, which are in agreement ( $\Delta\text{RV} < 2\sigma_{\text{RV}}$ , where  $\sigma_{\text{RV}}$  is the maximum error of the two measurements), and thus further indicates the likelihood of physical association. Of the remaining 59 companion candidates lacking Gaia DR2 measurements, 9 were previously



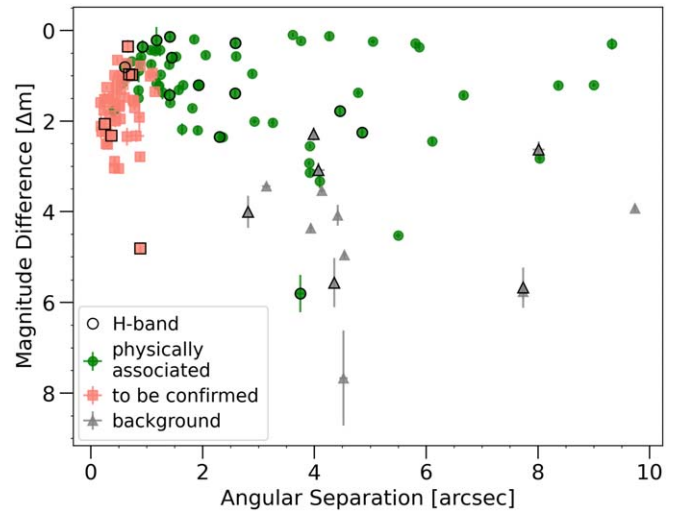
**Figure 4.** Comparing Gaia DR2 parallaxes and proper motions for primary stars and companion candidates to determine consistency for physical association. For reference, the comoving binaries identified in the Gaia DR2 binary catalog by Jiménez-Esteban et al. (2019) are also shown. For objects to be considered physically associated, we set the threshold for the ratios of primary – companion parallax difference to primary parallax ( $\Delta\pi/\pi_{\text{Primary}}$ ) and primary – companion proper motion difference to primary proper motion ( $\Delta\mu/\mu_{\text{Primary}}$ )  $< 0.35$  (dashed lines). In addition, we have Gaia DR2 RVs for three primary – companion pairs (star symbols), which all match within  $\Delta RV < 2\sigma_{RV}$ . Pairs with less reliable astrometry ( $RUWE > 1.4$ ) are marked in colored circles: red if the primary star’s  $RUWE > 1.4$ , yellow if the companion’s  $RUWE > 1.4$ , and orange if both  $RUWEs > 1.4$ .



**Figure 5.**  $RUWE$  values for the primary (colored by magnitude difference) and companion (gray, connected by a gray line to its primary) as a function of separation. A trend of large  $RUWE$  values ( $> 1.4$ , above the horizontal gray dashed line) for closer-in companions is visible; however, no particular trend with contrast is obvious.

studied systems reported in the literature as physically associated companions. Another five have astrometry measurements in Gaia EDR3,<sup>8</sup> three of which are physically associated companions and two are background objects. Therefore, a total of 62

<sup>8</sup> Gaia EDR3 was released after this paper was submitted. We have used this to update the physical association status of five companion candidates, which were previously unconfirmed with Gaia DR2. We also confirmed that the status of the other candidates remained unchanged. Except for these five companions, the properties reported throughout the paper are calculated using distances from Gaia DR2 astrometry.

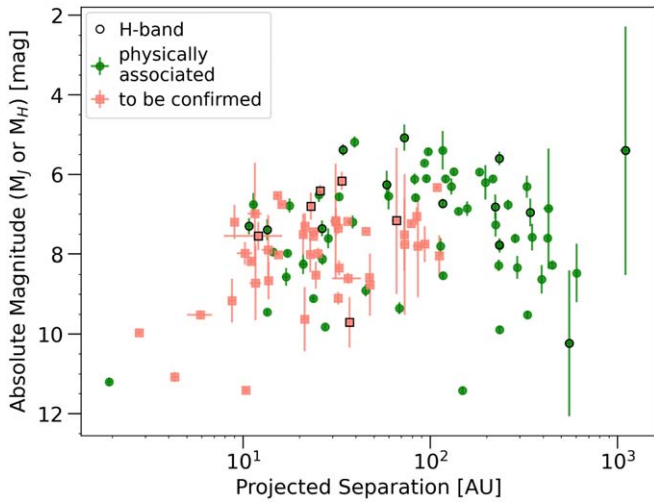


**Figure 6.** Summary of companion candidates detected with Robo-AO as part of this survey. Companions with Gaia DR2 parallaxes and proper motions consistent with their primary stars are determined to be physically associated (green circles). Companions not in Gaia DR2 or without parallax or proper motion information still need their physical association status to be determined (salmon squares). Companion candidates with parallax and proper motions inconsistent with the primary star were determined to be background objects (gray triangles). Measurements from Kitt Peak are in the  $J$  band and measurements from Maunakea are in the  $H$  band (markers outlined in black).

companions are physically associated, 14 are background objects, and 45 candidates will require future follow-up observations to assess their physical association.

We show the companion infrared contrasts and absolute magnitudes as a function of separation from the host star, with physical association status, in Figures 6 and 7. A summary of the physically associated companions in binary systems and their properties are shown in the Appendix, Table 7. Companion candidates where physical association has yet to be confirmed are summarized in the Appendix, Table 8. We display images of all of the confirmed and unconfirmed binary companions in Figures 8 and 9. For now, we assume the same parallax as the primary star to estimate their properties. Triple system candidates are summarized in Table 9 in the Appendix and further discussed in Section 4.1. As seen in both figures, most of the companions that do not have Gaia DR2 information are near the angular resolution limit of Gaia where accurate astrometry is more challenging. Hirsch et al. (2017) and Horch et al. (2014) have shown that the probability of a background star chance alignment decreases as the separation on-sky decreases. Therefore, we expect the majority of these close-in companion candidates to be physically associated.

We counted the stars surrounding each target with an unconfirmed companion candidate that were brighter than the faintest magnitude reached in all of the contrast curves ( $< 17$  in the  $J$  band and  $< 18$  in the  $H$  band). We conducted the search using the 2MASS catalog in a circular area of  $20'$  radius. We extrapolated the star count in each band beyond the 2MASS  $10\sigma$  sensitivity limits of 15.9 and 15.0 in the  $J$  and  $H$  bands, respectively. The UKIDSS catalog (Lawrence et al. 2007) reaches fainter IR magnitudes, avoiding the need to extrapolate. However, it does not cover the entire sky, and none of our targets with unconfirmed companion candidates were found in UKIDSS. We then divided the count by the search area in order to get the stellar surface density, then multiplied by the



**Figure 7.** Absolute magnitudes and projected physical separations of companion candidates. Color schemes are the same as in Figure 6. Candidates without enough information to determine physical association were assumed to be at the same distance as their host stars for the calculations. The majority of the unconfirmed candidates are within 100 au.

Robo-AO IR field of view to get the expected cumulative star counts within that area ( $N_{FOV}$ ). The probability of detecting at least one background object was then calculated assuming a Poisson distribution:

$$P(N_{\text{background}} \geq 1) = 1 - e^{-N_{\text{FOV}}}. \quad (7)$$

The resulting probabilities and their Poisson errors are reported in Tables 8 and 9. Only 5 of the 45 companion candidates have a >10% chance of a background star landing in the field of view of our observation. Of those, three are below 20%, and the remaining two values are both 43%. This reinforces our expectation that the vast majority of our companion candidates are true companions. However, it is important to note that although each individual companion candidate has a low probability of being a background object, this is not enough to claim that any specific companion candidate is not a background object. If we calculate the compound probability that at least one background object is detected around any of the 45 targets, we get a 93% probability.

### 3.2. Optical–Infrared Colors

For stars with simultaneous visible and infrared images, we report  $i' - J$  or  $i' - H$  colors for the companion candidates. For the 17 objects not detected in the visible images, we placed lower limits on their colors from the visible contrast limits. For companion candidates where a physical association has yet to be confirmed, we used these color measurements combined with absolute magnitudes and, assuming the companion is at the same distance as the primary, to determine whether their photometry is consistent with a low-mass companion or background star. We used evolutionary models (Chabrier et al. 2000; Baraffe et al. 2015) to estimate companion masses and temperatures from absolute magnitudes. In Figure 10, we show the companion candidates’ absolute magnitudes as a function of optical–infrared colors with their physical association status. We also show spectral type and mass estimates from stellar color–magnitude

sequences (Kraus & Hillenbrand 2007; Liu et al. 2016) and isochrone models (Chabrier et al. 2000; Baraffe et al. 2015). Companion candidates that are potentially substellar will be prioritized for follow-up observations (see Section 4.3).

### 3.3. Literature Search for Companions

We found 38 of our 121 companion candidates in previous catalogs, listed in the Appendix, Table 10. The following sections summarize the results.

#### 3.3.1. Robo-AO M-dwarf Multiplicity Survey

Lamman et al. (2020) surveyed 5566 field M dwarfs at visible wavelengths with Robo-AO to assess any multiplicity. They found 553 companion candidates within  $4''$  of 534 different stars. Seven of our companion candidates are also reported in this catalog.

#### 3.3.2. Imaging of CARMENES M Dwarfs

Cortés-Contreras et al. (2017) searched for low-mass companions to M dwarfs to vet targets for the CARMENES exoplanet survey. They observed 490 stars, from a volume-limited sample of M0–M5 stars within 14 pc. They found 80 bound companions and 6 companion candidates. We detected three of their confirmed companions. Due to a lack of Gaia DR2 measurements for two of those companions, the CARMENES input catalog was used to determine their physical association.

#### 3.3.3. Young Binaries and Lithium-rich Stars

Bowler et al. (2019) searched for new young, nearby, low-mass stars and report on spectroscopic observations of lithium-rich stars and binaries identified with Robo-AO. Nine of our companion candidates were identified with Robo-AO in this study, including two (2MASS J12115308+1249135 and 2MASS J15553178+3512028) identified as members of the young moving groups  $\beta$  Pic and Argus, respectively.

#### 3.3.4. Washington Double Star Catalog

We searched for our companions in the Washington Double Star (WDS) catalog (Mason et al. 2001). We found 27 of our companion candidates in the WDS, including 4 with an unconfirmed physical association and one that we ruled out as a background object (2MASS J02022823+1034533) but is listed in the WDS.

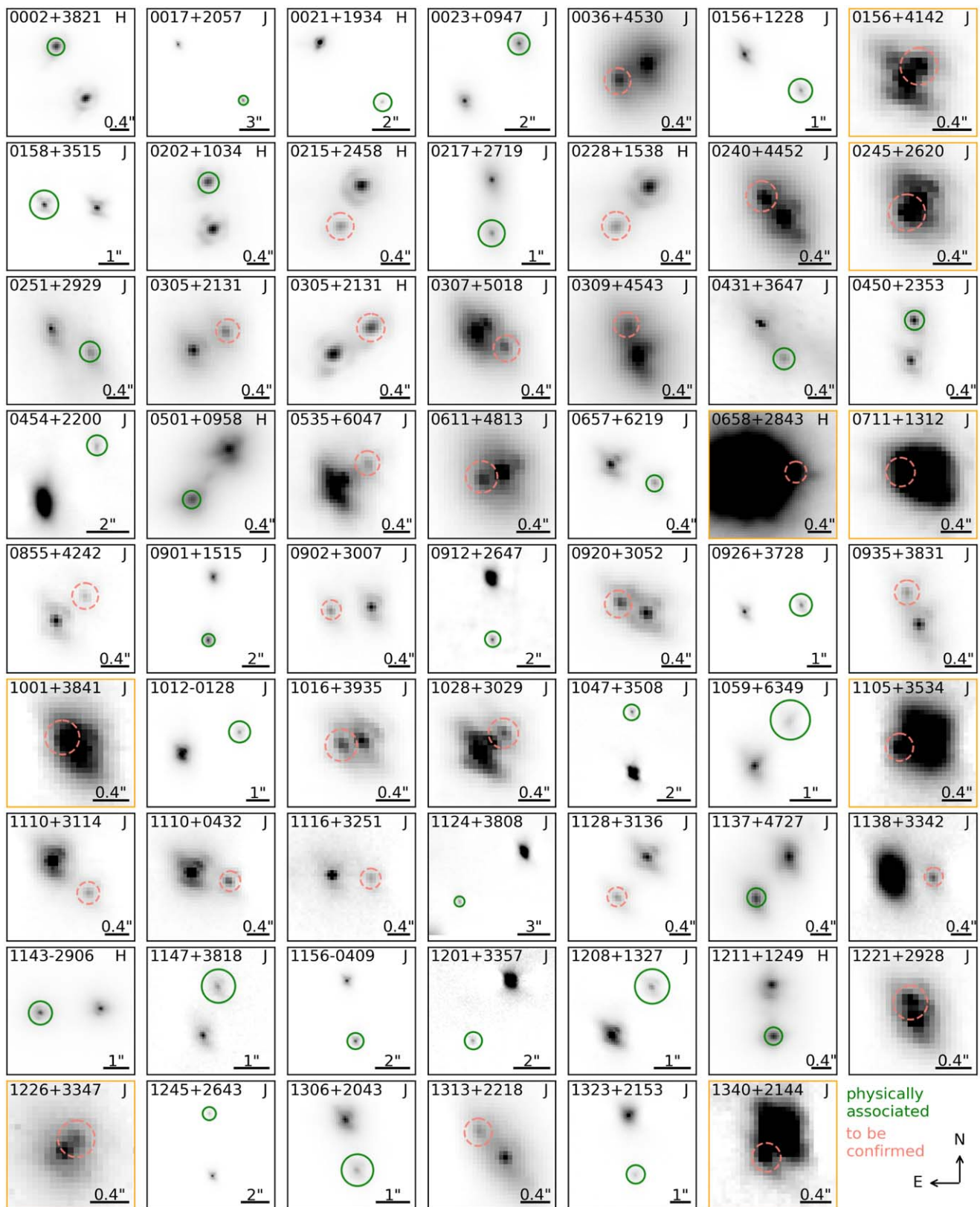
## 4. Discussion

### 4.1. Triple Systems

We discovered 10 triple system candidates, 6 of which include an object determined not to be physically associated from Gaia DR2 parallaxes and proper motions. Of the remaining four triple system candidates, three are known triples. The remaining system is potentially a new triple system, requiring follow-up observations to confirm.

The presence of a tertiary companion and resulting architecture of the system gives important insight into the formation and evolution of high-multiplicity systems. Hierarchical systems in particular, with a tight secondary and wider tertiary companion, have been shown to be the structure reached as orbits stabilize (Reipurth & Mikkola 2012).

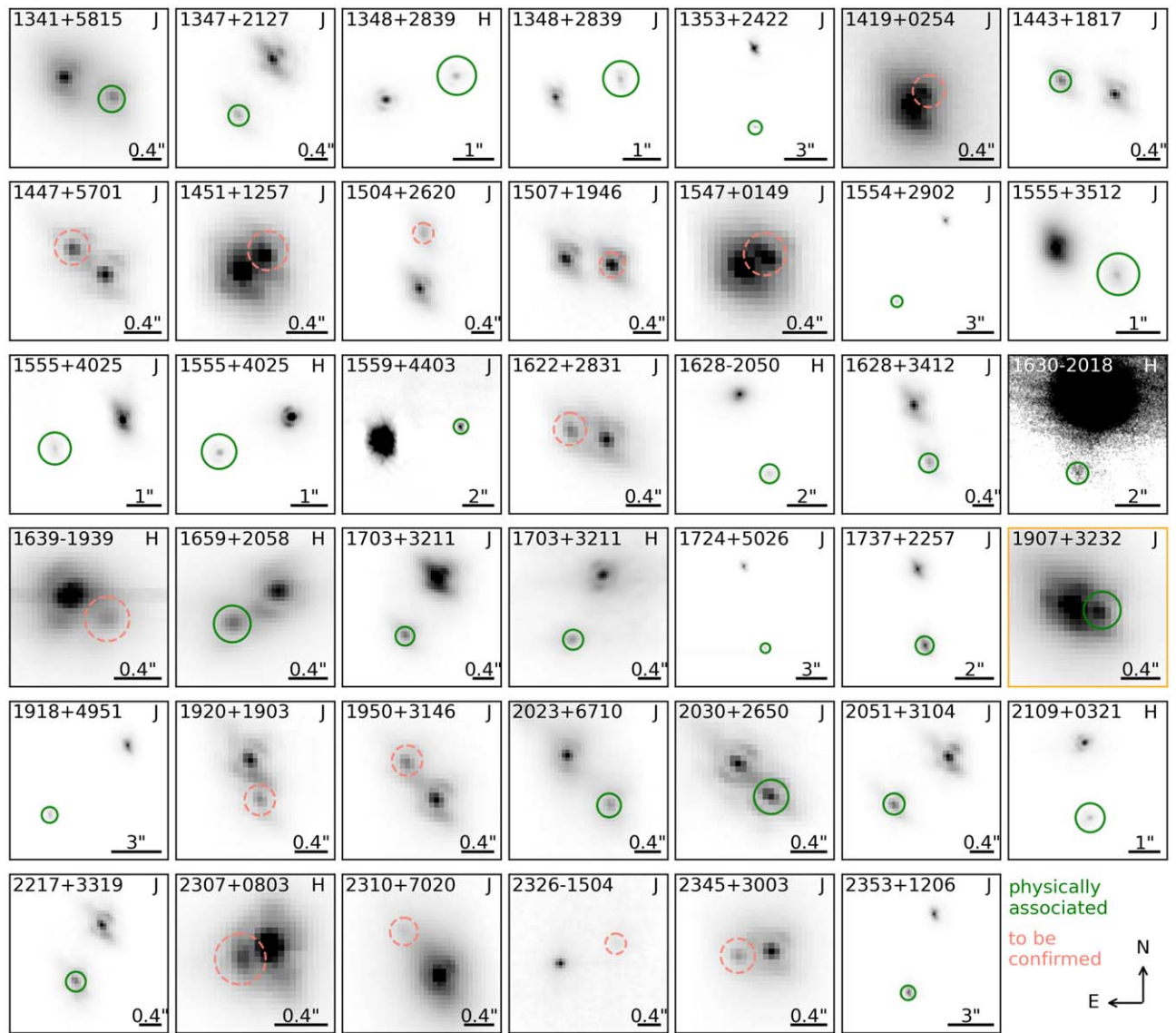




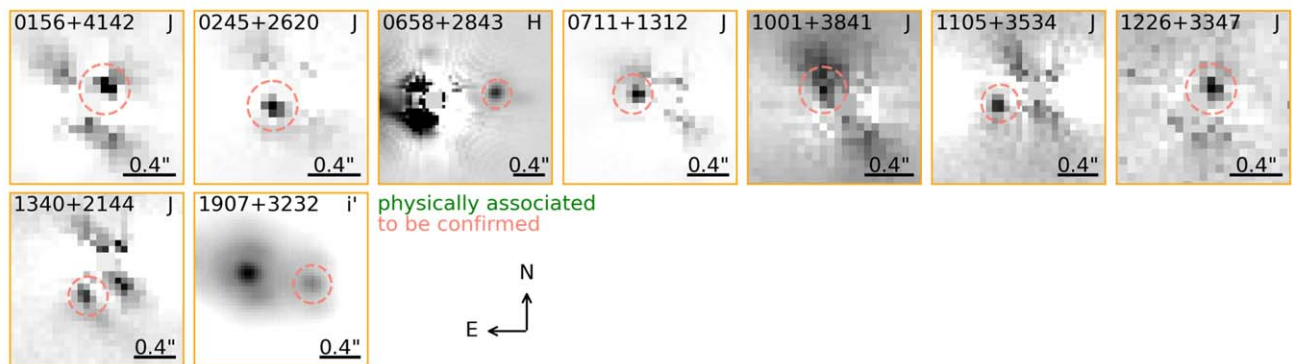
**Figure 8.** Linear-scale images of Robo-AO near-infrared binary detections of physically associated companions (green circles) and unconfirmed candidates (dashed salmon circles) with the dynamic range adjusted for companion visibility. The filter used for the observation is shown in the top right and the image scale is shown in the bottom right. Images outlined in orange are shown in Figure 9(b). Triple systems are shown in Figure 11.

Furthermore, the structure of our triple system candidates can help us infer which ones are more or less likely to be a true triple system with both companions physically associated.

Specifically, those that are not found in a hierarchical system are less likely to be true triple systems, because a hierarchical structure is the only stable structure.



(a)

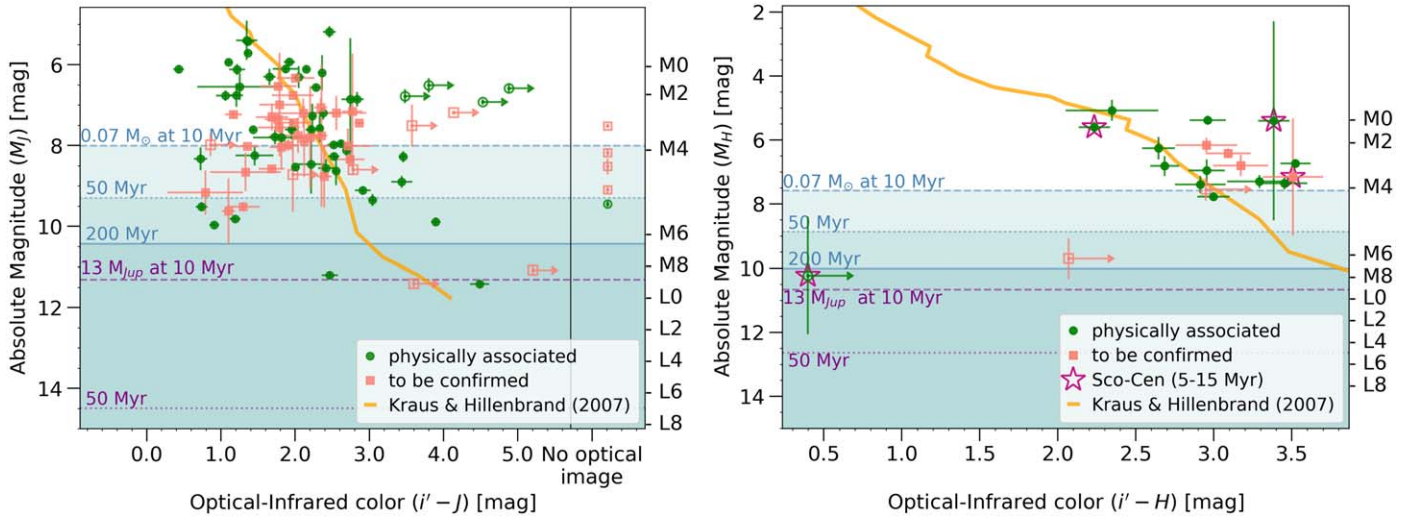


(b)

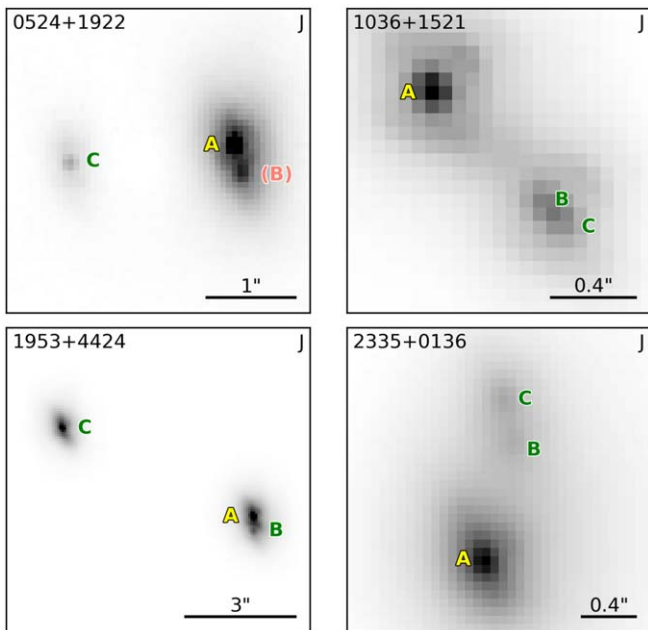
**Figure 9.** (a) Linear-scale images of Robo-AO near-infrared binary detections of physically associated companions (green circles) and unconfirmed candidates (dashed salmon circles) with the dynamic range adjusted for companion visibility. The filter used for the observation is shown in the top right and the image scale is shown in the bottom right. Images outlined in orange are shown in (b). Triple systems are shown in Figure 11. (b) Radially subtracted images for very close companion candidates not easily seen in Figures 8 and 9(a). Except for 2MASS J19074283+3232396 where it is most easily seen in the  $i'$ -band image.

Images of the four triple system candidates are shown in Figure 11, and each system is detailed below, the known systems first followed by the new candidate system.

2MASS J10364483+1521394 is an M4.5 rotational variable star with flares (Rodríguez Martínez et al. 2020) and is a triple system at a distance of 19.75 pc. We detect the companions at



**Figure 10.** Companion candidate absolute  $J$  (left) and  $H$  (right) magnitudes as a function of optical–infrared colors. Targets with a companion candidate detected in the infrared but not in the visible are shown with lower limits on their colors, denoted by open symbols with arrows. Companions without  $i'$ -band photometry are shown as salmon squares. Companions that are physically associated are shown in green circles, while those that still need to be confirmed are shown as salmon squares. Corresponding mass estimates from isochrones of 10, 50, and 200 Myr are shown to delineate the stellar–substellar boundary (shaded blue area) and the deuterium burning limit (purple dashed and dotted lines). Companion candidates in the Sco-Cen sample are outlined with a pink star. We estimated the spectral types using the stellar SEDs in Kraus & Hillenbrand (2007) for types earlier than M6 and Liu et al.’s (2016) linear relation for M6–L8 field objects.



**Figure 11.** Images of the triple system candidates. The companions that were determined to be physically associated, either from Gaia DR2 astrometry or from the literature, are labeled “B” or “C” in green, while the one whose physical association has yet to be confirmed is labeled “(B)” in salmon. The primary star is labeled with a yellow “A.” The 2MASS ID and the Robo-AO IR filter are shown in the upper left and right, respectively. The images are displayed in linear stretch with the dynamic range adjusted for the faintest companion visibility. North is up and east is left.

projected separations of 14.82 au and 17.78 au, with the companions forming a nearly equal-mass binary at a projected separation of  $0''.15$  (3 au). Calissendorff et al. (2017) recently analyzed the orbits and masses of this known triple system.

2MASS J19535443+4424541 is a known hierarchical triple system (Tokovinin 2017), with a tight central binary and a farther-out fainter companion. The primary is an M5.5Ve star, in a tight binary with a  $\sim 0.1 M_{\odot}$  companion and the wider

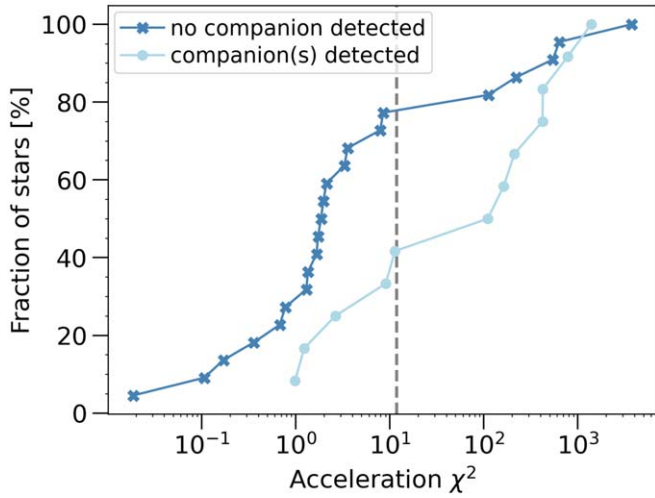
companion is an M6V star. This is one of the nearest triple systems, at a distance of 4.7 pc. The inner binary is separated by 1.9 au and the outer companion is at a separation of 27.2 au. Tokovinin (2017) determined the inner binary to have a period of 15.2 yr and eccentricity of 0.32 and the outer companion’s orbit direction is retrograde.

2MASS J23350028+0136193 is a K7V star at a distance of 18.2 pc and a member of the IC 2391 moving group with an age estimate of  $50 \pm 5$  Myr (Barrado y Navascués et al. 2004; Faherty et al. 2018). This is a triple system, with recent measurements on the fainter and closer companion reported in Mann et al. (2019) and Kammerer et al. (2019). The projected separation of the companions are 17.70 and 25.37 au. Mann et al. (2019) report a total system mass of  $0.606 \pm 0.018 M_{\odot}$ . Kammerer et al. (2019) report an RV of  $4.5 \text{ km s}^{-1}$  in the HARPS RV survey.

2MASS J05242572+1922070 is a weak-line T Tauri star (Li & Hu 1998) and a disk-free member of the Taurus-Auriga star-forming complex (Kraus et al. 2017) at a Gaia DR2 distance of  $58.34 \pm 1.01$  pc. The outer companion is at a projected separation of  $113.2 \pm 1.3$  au, and we have determined it to be physically associated from Gaia DR2 proper motion and parallax measurements. Using isochrone models, we estimate its mass to be  $84\text{--}319 M_{\text{Jup}}$  for an age range of 10–200 Myr. The inner companion candidate is at a projected separation of  $20.9 \pm 0.7$  au and remains to be confirmed. However, we expect this system to be a true new triple system given the overall hierarchical appearance of the system, the companion candidate’s very close separation ( $0''.36$ ), the primary star’s RUWE value  $> 1.4$  (3.6 in Gaia DR2 and 1.8 in Gaia EDR3), and the low probability of a chance alignment with a background star ( $7.95\% \pm 0.13\%$ ).

#### 4.2. Accelerating Stars

The Hipparcos–Gaia Catalog of Accelerations (HGCA; Brandt 2018) measured accelerations by using three proper motion and positional measurements from Hipparcos (near



**Figure 12.** Cumulative distribution of acceleration  $\chi^2$  values for stars in the HGCA catalog comparing stars with no Robo-AO companion detections to those with companion candidates. Stars with  $\chi^2 > 11.8$  are accelerating with  $>3\sigma$  significance. A larger proportion,  $58^{+12}_{-14}\%$  (7/12), of stars with companion detections are accelerating than those with no companion detection,  $23^{+11}_{-6}\%$  (5/22).

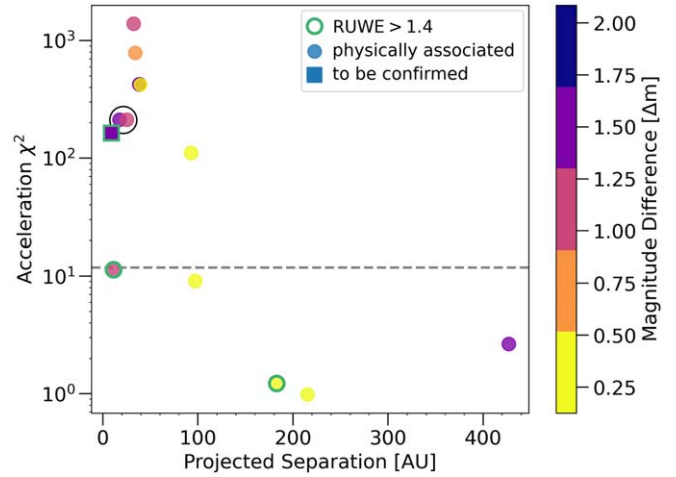
epoch 1991.25), Gaia DR2 (near epoch 2015.5), and the Gaia–Hipparcos scaled positional difference over the 24 yr baseline. Stars with measured accelerations are particularly interesting as they can provide dynamical masses and orbits for companions (Brandt et al. 2019). We consider stars with  $\chi^2 > 11.8$ , corresponding to  $3\sigma$ , calculated from the Gaia proper motions against the Gaia–Hipparcos, to have significant accelerations. Of our observed targets, 34 are found in the HGCA catalog: 22 with no imaged companion and 12 with imaged companion candidate(s). The cumulative distribution of acceleration  $\chi^2$  are shown in Figure 12.

Of the observed stars found in the HGCA catalog where we did not detect a companion,  $77^{+6}_{-11}\%$  (17/22) do not have significant accelerations ( $\chi^2 < 11.8$ ), and  $23^{+11}_{-6}\%$  (5/22) have significant accelerations. Of those five stars, two are reported in the literature as having a tight companion: 2MASS J13232325+5754222 (Horch et al. 2017) and 2MASS J22372987+3922519 (Pourbaix et al. 2004). It is possible that there are also unresolved companions around the remaining three stars with significant acceleration measurements but where we do not detect any companions.

In contrast, for the stars with companion detection(s),  $58^{+12}_{-14}\%$  (7/12) have significant accelerations and  $42^{+14}_{-12}\%$  (5/12) do not. The  $1\sigma$  uncertainties are numerically calculated following the binomial distribution, as described in Burgasser et al. (2003). Figure 13 shows that there is a clear correlation between acceleration significance and companion projected separation, as expected. Similarly, the companion that does not have Gaia DR2 measurements but has significant acceleration (2MASS J03093085+4543586) is very likely to be a physically associated companion.

#### 4.3. Substellar Candidates

While the majority of our detections are very likely stellar companions, a handful are potentially substellar. We do not have precise age estimates for most of our targets; therefore, these systems will require additional infrared color photometry



**Figure 13.** Target acceleration significance from the HGCA catalog as a function of companion projected separation. The threshold determining “significant acceleration” is placed at  $\chi^2 > 11.8$  (dashed gray line), and targets with large RUWE values, and thus less reliable astrometry, are outlined in green. Targets with companions that have been confirmed to be physically associated are marked as circles and the one that still needs to be confirmed is marked as a square but is highly likely to be physically associated due to its high acceleration significance. One system is a triple system, and its two companions are circled in black. A correlation is apparent where closer companions have large acceleration significances.

and spectroscopy to characterize these objects and determine their spectral types. Table 4 summarizes the companions we detected with Robo-AO in LASSO that have already been discovered and characterized but would have been flagged as potentially substellar and needing follow-up study from the Robo-AO data.

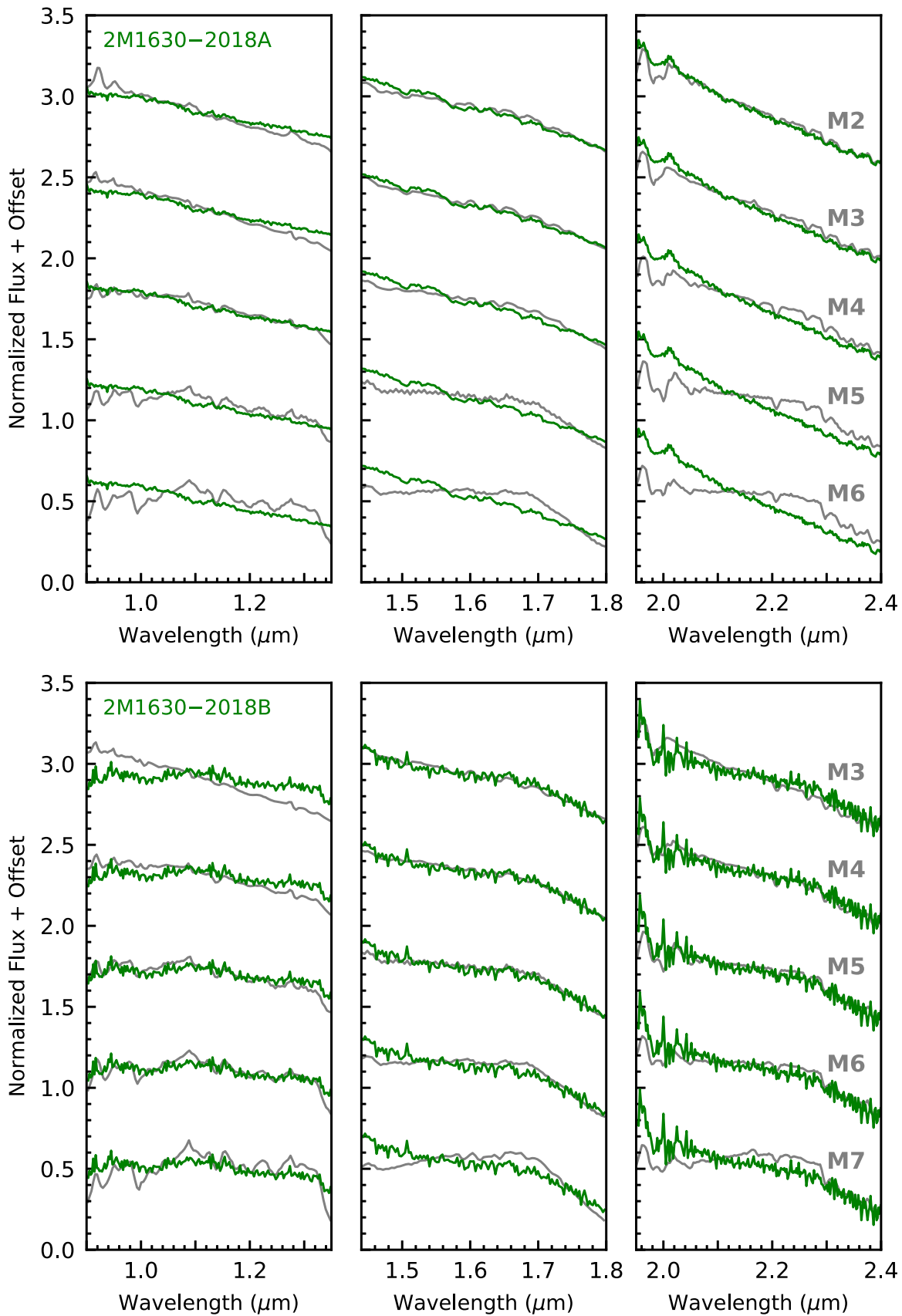
Below we summarize companions not characterized in the literature:

2MASS J06584690+2843004 is an M-type star at a Gaia-determined distance of  $41.75 \pm 1.2$  pc. We detect a companion candidate at a separation of  $0''.88$ . We found no match in Gaia DR2 for the companion, so follow-up is needed to confirm whether it is physically associated. We do not detect it in the visible image so we place a minimum  $i' - H$  color limit of 2.07 mag. Using isochrone models, we estimate its mass to be  $17\text{--}86 M_{\text{Jup}}$  for an age range of 10–200 Myr.

2MASS J12082885+1327090 is at a distance of  $37.49 \pm 0.11$  pc. We find a physically associated companion at  $1''.8$  or a projected separation of 68.43 au. Its  $i' - J$  color is 3.04 mag corresponding to an estimated SpT of M6.6 from Kraus & Hillenbrand (2007) SEDs. By using PanSTARRS photometry we determine this object is red with  $g - r$  and  $z - y$  colors of 2.07 and 0.96, respectively. Using the color and spectral type estimates from Best et al. (2018), this object would be a late-M/early-L-type object. Its isochrone mass range for 10–200 Myr is  $21\text{--}135 M_{\text{Jup}}$ .

2MASS J14192958+0254365 is an M5 star at a distance of  $20.83 \pm 0.04$  pc. We detect a companion candidate at  $0''.5$  with a S/N of 6.7, just above our detection threshold of 5. We do not detect it in the visible image, thus placing an  $i' - J$  color limit of  $>3.6$  mag and late-M spectral type. We do not detect the companion in Gaia DR2.

2MASS J15471513+0149218 is at a distance of  $18.39 \pm 0.14$  pc. We detect a companion candidate at a separation of  $0''.23$ , with no detection in the visible camera, corresponding to an  $i' - J$  color limit of 5.2 mag. Using isochrone models, we



**Figure 14.** IRTF/SpEx spectra of 2M1630A (top) and 2M1630B (bottom) as compared to the Kirkpatrick et al. (2010) M-dwarf spectral standards (gray) in the *J*, *H*, and *K* bands. All these standards are normalized by the averaged flux of our targets within each band and their names are Gl 91 (M2), Gl 752A (M3), Gl 213 (M4), Gl 51 (M5), LHS 1375 (M6), and vB 8 (M7). We derive a visual near-infrared spectral type of  $M3.5 \pm 1$  and  $M5 \pm 1$  for the primary and the companion, respectively.

**Table 4**  
LASSO Companions Found in the Literature

2MASS ID	SpT		Mass	References <sup>a</sup>
	Prim	Comp		
06575703+6219197	M4	M5	...	1
11240434+3808108	M4.5	M9.5	$81 \pm 5 M_{\text{Jup}}$	2, 3
15553178+3512028	M4	M7	...	4
15594729+4403595	M1.5	$M7.5 \pm 0.5$	$43 \pm 9 M_{\text{Jup}}$	5, 3
19074283+3232396	...	...	$0.42 \pm 0.03 M_{\odot}^b$	6
20231789+6710096	M5	M5	...	7

**Note.**

<sup>a</sup> This is the total system mass ( $M_{\text{tot}}$ ).

<sup>b</sup> **References.** (1) Newton et al. (2014), (2) Close et al. (2003), (3) Bowler et al. (2015b), (4) WDS catalog, (5) Janson et al. (2012), (6) Mann et al. (2019), (7) Law et al. (2008).

estimate its mass to be  $14\text{--}56 M_{\text{Jup}}$  for an age range of 10–200 Myr. PanSTARRS detects a very blue object at a projected separation of  $\sim 4''$  and PA of  $\sim 300^\circ$ . It is unassociated according to Gaia DR2 measurements and cataloged as a white dwarf by Bai et al. (2018). This blue object is too faint for both the visible and infrared Robo-AO cameras.

2MASS J16304072-2018186 is a member of Sco-Cen and thus very young (5–15 Myr) compared to most of our other targets and at a distance of  $182.82 \pm 4.27$  pc. We detected two nearby objects, also detected by Gaia DR2. The Gaia data indicate that only one is a physically associated companion at a projected separation of 551.63 au while the other one is a background object. These objects are visible in PanSTARRS data, which measures the physical companion as a very red object. We obtained near-infrared spectra of both the primary star (2M1630-2018A) and the physically associated companion (2M1630-2018B) using the NASA Infrared Telescope Facility (IRTF) in prism mode on 2020 August 23 UT. We took eight exposures for both objects in an ABBA pattern with 10 and 120 s each for the primary and companion, respectively, and we contemporaneously observed a nearby AOV standard star HD 152071 for telluric correction. We reduced the data using `Spextool` version 4.1 (Cushing et al. 2004), and our resulting spectra have a median S/N of 215 per pixel for the primary and 55 per pixel for the companion in the *J* band. Comparing these objects' spectra with M-type spectral standards from Kirkpatrick et al. (2010) in each of the *J*, *H*, and *K* bands, we derive visual near-infrared spectral types of  $M3.5 \pm 1$  and  $M5 \pm 1$  for the primary and companion, respectively (Figure 14). Quantitative spectral types are not available for these objects as their  $\text{H}_2\text{O}$ -band spectral indices exceed the applicable range of the Allers & Liu (2013) and Zhang et al. (2018) methods.

#### 4.4. Survey Yields and Expectations

This is an ongoing survey and a detailed statistical analysis of these results is beyond the scope of this paper. We calculate the raw multiplicity detection frequency of the 427 stars we observed, excluding detections ruled out as background objects, and including companions where physical association is to be determined. The fraction of observed stars with companion(s) is  $24.1\% \pm 2.4\%$  (half still need confirmation). The breakdown of multiplicity fractions between the young field stars and Sco-Cen association stars are summarized in Table 5. Uncertainties are calculated following the binomial

**Table 5**  
Companion Detection Frequencies

Sample	# Stars Observed	# Stars with Companion(s)	
Total	427	103	$(24.1\% \pm 2.4\%)$
Total young field	403	99	$(24.6\% \pm 2.5\%)$
LASSO young field	321	70	$(21.8\% \pm 2.6\%)$
Pre-LASSO young field	82	29	$(35^{+6}_{-5}\%)$
Sco-Cen association	24	4	$(17^{+10}_{-5}\%)$

distribution for samples with  $<100$  stars and the Poisson distribution for the larger samples.

Cool dwarfs have lower multiplicity fractions than higher-mass stars (Dupuy et al. 2013) with fractions of  $26\% \pm 3\%$  for stars  $0.1\text{--}0.7 M_{\odot}$  (Duchêne & Kraus 2013), consistent with our results. Our Sco-Cen sample is an order of magnitude smaller than our young field sample, so a detailed statistical comparison of our young field sample and our younger Sco-Cen sample is beyond the scope of this paper. We also note the difference in detection frequencies between our LASSO and pre-LASSO samples. The pre-LASSO sample was constructed using photometric distances, which would increase the chances of inadvertently including more distant binaries, thought to be less distant single stars. The fraction of higher-order systems is  $0.9\% \pm 0.5\%$ . Winters et al. (2019) estimate a higher-order multiplicity rate of  $\sim 5\%$ , from a companion search at separations of  $2''\text{--}300''$ , which is over an order of magnitude larger than our field of view, where many of the wide-orbit tertiary companions would be.

One bona fide substellar object and one companion at the substellar–stellar mass boundary were detected in our survey (2MASS J15594729+4403595 and 2MASS J11240434+3808108) and another  $\sim 5$  are potentially substellar. This gives us a detection rate of  $0.5\%\text{--}1.5\%$ . This is somewhat lower than the current overall frequency estimates of  $1\%\text{--}4\%$  (Bowler & Nielsen 2018) for  $13\text{--}75 M_{\text{Jup}}$  companions. This is likely because we did not have the sensitivity necessary to detect substellar objects in all of our observations (see Figure 3). The dome seeing fluctuated throughout the survey, affecting the AO performance. In addition, we do not have precise age estimates for most of our targets, especially those not part of young moving groups. Kastner et al. (2018) discuss

the UV-excess selection method for youth that we followed may not only be selecting stars as young as we expect. They investigated a sample of 400 low-mass (K- and early-M-type) stars expected to be young from UV excess and with isochrone ages  $\lesssim 80$  Myr. However, a portion of those stars were fainter in the X-ray than expected, which could suggest they are not as young as expected.

## 5. Conclusion

The ongoing LASSO survey is one of the largest direct imaging surveys searching for wide-orbit substellar companions. The goal is to study the demographics of wide-orbit substellar companion populations in order to better understand their formation and evolution mechanisms.

We have observed 427 young, nearby, low-mass stars with Robo-AO on the 2.1 m telescope on Kitt Peak, Arizona, and on the UH 2.2 m telescope on Maunakea, Hawai‘i, simultaneously in the visible and near-infrared. Our main findings are summarized below:

1. We detected 121 companion candidates and determined that 62 are likely physically associated from Gaia DR2 and EDR3 common parallax and proper motion measurements and a literature search. Another 45 have yet to be confirmed, though we expect most of them to also be physically associated. The remaining 14 are background objects.
2. We were sensitive to substellar companions for 50% of our LASSO field observations for separation ranges of 50–450 au and for 90% of our Sco-Cen observations for separation ranges of 210–570 au.
3. Four triple system candidates were detected, three of which have been previously reported in the literature.
4. We detected one bona fide brown dwarf, one companion at the threshold between brown dwarf and stellar mass, and another five companion candidates that will require follow-up observations to determine their nature.
5. The range of projected separations spans 2–1101 au and masses  $\gtrsim 43 M_{\text{Jup}}$ .
6. We investigated accelerations calculated from Hipparcos–Gaia proper motion measurements and found that a higher fraction ( $58^{+12}_{-14}\%$ ) of stars with companions are accelerating compared to stars without detected companions ( $23^{+11}_{-6}\%$ ). These accelerating stars with detected companions will allow us to calculate dynamical masses with future orbit monitoring.
7. Our multiplicity fractions are  $24.1\% \pm 2.4\%$  for the entire sample,  $24.6 \pm 2.5\%$  for the young field stars, and  $17^{+10}_{-5}\%$  for the Sco-Cen sample.

The authors are honored to be permitted to conduct astronomical research on Iolka Du‘ag (Kitt Peak), a mountain with particular significance to the Tohono O‘odham Nation. The authors also wish to recognize and acknowledge the very significant cultural role and reverence that the summit of Maunakea has always had within the indigenous Hawaiian community. We are most fortunate to have the opportunity to conduct observations from both mountains.

We are grateful to the Kitt Peak National Observatory and UH88" staff for their support of Robo-AO on the 2.1 m and 2.2 m telescopes, respectively. We thank Shri Kulkarni for his sustained backing of Robo-AO through all its iterations, Dani

Atkinson for help understanding the intricacies of the SAPHIRA detectors, and Bo Reipurth for valuable discussions and comments on the manuscript. We are grateful to Adwin Boogert for observing 2MASS J16304072-2018186 and its companion with IRTF/SpeX.

The Robo-AO system is supported by collaborating partner institutions, the California Institute of Technology and the Inter-University Centre for Astronomy and Astrophysics, and by the National Science Foundation under grant Nos. AST-0906060, AST-0960343, and AST-1207891, by the Mount Cuba Astronomical Foundation, and by a gift from Samuel Oschin. As part of the development of Robo-AO-2, Robo-AO at the UH 2.2 m telescope system is supported by the National Science Foundation under grant No. AST-1712014, the State of Hawaii Capital Improvement Projects, and by a gift from the Lumb Family.

M.C.L. acknowledges support from National Science Foundation grant AST-1518339.

B.P.B. acknowledges support from the National Science Foundation grant AST-1909209.

This work has made use of data from the European Space Agency (ESA) mission Gaia (<https://www.cosmos.esa.int/gaia>), processed by the Gaia Data Processing and Analysis Consortium (DPAC, <https://www.cosmos.esa.int/web/gaia/dpac/consortium>). Funding for the DPAC has been provided by national institutions, in particular the institutions participating in the Gaia Multilateral Agreement.

This research has made use of the VizieR catalog access tool, CDS, Strasbourg, France (DOI:10.26093/cds/vizieR). The original description of the VizieR service was published in A&AS 143, 23.

This research has made use of the SIMBAD database, operated by Centre des Données Stellaires (Strasbourg, France), and bibliographic references from the Astrophysics Data System maintained by SAO/NASA.

This publication has made use of data products from the Two Micron All Sky Survey, which is a joint project of the University of Massachusetts and the Infrared Processing and Analysis Center/California Institute of Technology, funded by the National Aeronautics and Space Administration and the National Science Foundation.

This research has made use of the SVO Filter Profile Service (<http://svo2.cab.inta-csic.es/theory/fps/>) supported from the Spanish MINECO through grant AYA2017-84089.

This research has made use of the Washington Double Star Catalog maintained at the US Naval Observatory.

*Facility:* KPNO:2.1 m (Robo-AO), UH:2.2 m (Robo-AO), IRTF (SpeX).

*Software:* ExoDMC (v1.1b; Bonavita 2020), Spextool (v4.1; Cushing et al. 2004).

## Appendix

Table 6 lists Robo-AO companion detection measurements and, when available, Gaia DR2 measurements. Tables 7–9 list the properties calculated for physically associated binaries, unconfirmed binary candidates, and triple systems, respectively. Table 10 lists the Robo-AO-detected companions that are found in other catalogs (Cortés-Contreras et al. 2017; Bowler et al. 2019; Lamman et al. 2020, and WDS). Finally, Table 11 lists all observed targets reported in this work.

**Table 6**  
Companion Candidate Detection Measurements

Primary 2MASS ID	Separation ( $''$ )	P. A. ( $^{\circ}$ )	Robo-AO			Detection S/N			Gaia DR2			Phys. assoc.	RUWE prim. (comp)	HIP-Gaia prim. $\chi^2_{\text{acc}}$
			Magnitude Difference ( $\Delta m$ )			$i'$	$J$	$H$	$i'$	$J$	$H$			
00024011+3821453 B	1.41 ± 0.03	26.5 ± 0.6	0.2 ± 0.04	...	0.14 ± 0.1	390	...	119	0.17	10 <sup>-2</sup>	10 <sup>-2</sup>	yes	4.1 (10.7)	...
00175864+2057192 B	9.33 ± 0.02	232.4 ± 0.1	0.55 ± 0.0	0.3 ± 0.13	...	653	195	...	0.59	10 <sup>-3</sup>	10 <sup>-3</sup>	yes	1.0 (1.2)	...
00213183+1934253 B	4.86 ± 0.02	224.3 ± 0.4	3.1 ± 0.02	...	2.25 ± 0.1	483	...	207	3.1	10 <sup>-3</sup>	0.1	yes	1.3 (1.2)	...
00233382+0947356 B	3.61 ± 0.01	316.4 ± 0.2	...	0.09 ± 0.05	...	...	116	...	-0.29	10 <sup>-3</sup>	10 <sup>-2</sup>	yes	1.2 (1.3)	...
00360847+4530575 B	0.52 ± 0.02	120.9 ± 1.3	...	1.65 ± 0.08	...	...	19	...	...	...	...	...	...	...
01563544+1228047 B	2.89 ± 0.02	240.4 ± 0.4	1.24 ± 0.01	0.96 ± 0.08	...	344	116	...	1.46	0.2	10 <sup>-3</sup>	yes	5.5 (1.0)	...
01564996+4142303 B	0.19 ± 0.03	315.9 ± 5.2	2.36 ± 0.2	2.23 ± 0.1	...	7	4	...	...	...	...	...	1.6	...
01584363+3515281 B	1.85 ± 0.01	86.3 ± 0.3	...	0.2 ± 0.07	...	...	131	...	-0.06	10 <sup>-2</sup>	0.1	yes	2.4 (1.5)	...
02022823+1034533 C	3.99 ± 0.02	185.9 ± 0.3	1.39 ± 0.02	...	2.29 ± 0.15	602	...	218	0.99	0.9	0.8	no	4.9	...
02022823+1034533 B	0.93 ± 0.01	3.1 ± 0.8	0.62 ± 0.07	...	0.36 ± 0.15	213	...	68	0.46	10 <sup>-2</sup>	10 <sup>-2</sup>	yes	4.9 (11.3)	...
02154870+2458501 B	0.69 ± 0.02	150.1 ± 1.1	1.67 ± 0.03	...	0.97 ± 0.19	138	...	49	...	...	...	...	2.0	...
02170213+2719305 B	2.05 ± 0.01	183.6 ± 0.4	0.37 ± 0.01	0.54 ± 0.07	...	306	72	...	0.08	10 <sup>-3</sup>	10 <sup>-2</sup>	yes	0.9 (1.3)	...
02284694+1538535 B	0.73 ± 0.02	137.9 ± 1.2	1.58 ± 0.03	...	0.98 ± 0.14	162	...	48	1.51	...	...	...	1.9	...
02405251+4452365 B	0.39 ± 0.02	48.5 ± 1.9	1.31 ± 0.07	1.61 ± 0.51	...	57	12	...	...	...	...	...	5.0	...
02453008+2620233 B	0.18 ± 0.01	141.9 ± 6.1	2.35 ± 0.23	1.59 ± 0.15	...	23	7	...	...	...	...	...	19.7	...
02514973+2929131 B	0.89 ± 0.04	243.6 ± 5.0	0.72 ± 0.21	0.58 ± 0.14	...	146	31	...	...	...	...	yes <sup>b</sup>	12.1	...
03051963+2131219 B	0.66 ± 0.02	301.2 ± 1.5	1.66 ± 0.08	1.01 ± 0.31	...	94	28	...	...	...	...	...	6.8	...
03051963+2131219 B	0.67 ± 0.01	304.0 ± 1.5	0.91 ± 0.1	...	0.35 ± 0.15	140	...	65	...	...	...	...	6.8	...
03072749+5018081 B	0.53 ± 0.01	243.8 ± 2.3	2.84 ± 0.03	1.95 ± 0.14	...	52	16	...	...	...	...	...	...	...
03093085+4543586 B	0.51 ± 0.02	20.2 ± 3.0	2.4 ± 0.14	1.68 ± 0.38	...	63	18	...	...	...	...	...	38.8	162.6
04310001+3647548 B	0.78 ± 0.01	217.0 ± 0.8	0.88 ± 0.03	0.97 ± 0.08	...	118	25	...	0.46	0.3	0.3	yes	10.8 (6.4)	...
04504680+2353317 B	0.86 ± 0.02	358.2 ± 1.0	0.75 ± 0.51	0.89 ± 0.25	...	140	28	...	0.13	10 <sup>-2</sup>	0.1	yes	1.6 (2.4)	...
04540567+2200545 B	3.92 ± 0.02	318.6 ± 0.3	2.3 ± 0.03	3.14 ± 0.08	...	72	79	...	4.02	0.1	0.1	yes	36.0 (1.1)	...
05015881+0958587 B	1.45 ± 0.01	141.9 ± 0.7	0.84 ± 0.03	...	0.6 ± 0.11	314	...	92	0.83	10 <sup>-3</sup>	10 <sup>-2</sup>	yes	1.3 (3.2)	783.1
05242572+1922070 C	1.91 ± 0.02	99.0 ± 1.2	2.49 ± 0.37	2.21 ± 0.09	...	75	64	...	1.95	10 <sup>-2</sup>	0.2	yes	3.6 (3.1)	...
05242572+1922070 B	0.36 ± 0.01	200.6 ± 2.1	...	1.88 ± 0.29	...	...	9	...	...	...	...	...	3.6	...
05354082+6047451 B	0.64 ± 0.03	305.0 ± 1.4	...	2.35 ± 0.2	...	...	12	...	...	...	...	...	4.1	...
06014571+1305015 B	3.93 ± 0.03	13.8 ± 0.2	3.72 ± 0.05	4.37 ± 0.09	...	148	96	...	3.79	1.0	1.0	no	0.9 (1.1)	...
06114391+4813113 B	0.26 ± 0.01	104.1 ± 2.5	...	2.24 ± 0.05	...	...	7	...	...	...	...	...	12.7	...
06575703+6219197 B	1.17 ± 0.01	248.1 ± 0.6	...	1.17 ± 0.07	...	...	53	...	1.43	10 <sup>-3</sup>	0.1	yes	1.2 (5.7)	...
06584690+2843004 B	0.89 ± 0.02	275.5 ± 1.7	...	...	4.82 ± 0.13	...	...	9	...	...	...	...	18.8	...
07110918+1312442 B	0.3 ± 0.02	85.8 ± 2.6	2.94 ± 0.08	2.52 ± 0.05	...	31	8	...	...	...	...	...	35.8	...
08551482+4242427 B	0.6 ± 0.01	312.9 ± 1.1	1.86 ± 0.02	1.48 ± 0.08	...	67	17	...	...	...	...	...	13.8	...
09011748+1515523 B	5.05 ± 0.04	178.1 ± 0.3	0.17 ± 0.01	0.24 ± 0.05	...	242	112	...	0.18	10 <sup>-3</sup>	10 <sup>-2</sup>	yes	0.9 (1.1)	110.2
09021527+3007590 B	0.89 ± 0.03	98.1 ± 1.4	1.11 ± 0.25	0.78 ± 0.05	...	120	33	...	...	...	...	...	...	...
09124007+2647327 B	3.92 ± 0.01	183.5 ± 0.2	3.51 ± 0.03	2.55 ± 0.05	...	71	121	...	3.03	10 <sup>-3</sup>	10 <sup>-2</sup>	yes	1.1 (1.2)	...
09200048+3052397 B	0.43 ± 0.02	71.3 ± 1.6	1.03 ± 0.23	0.99 ± 0.08	...	65	18	...	...	...	...	...	...	...
09261352+3728253 B	2.6 ± 0.02	279.5 ± 0.3	0.29 ± 0.0	0.57 ± 0.08	...	328	103	...	0.29	10 <sup>-3</sup>	10 <sup>-2</sup>	yes	1.3 (1.3)	...
09354051+3831339 B	0.56 ± 0.02	21.5 ± 3.2	0.6 ± 0.2	1.08 ± 0.05	...	46	18	...	...	...	...	...	...	...
10013178+3841174 B	0.27 ± 0.01	34.6 ± 3.1	1.6 ± 0.03	2.51 ± 0.08	...	18	4	...	...	...	...	...	7.2	...
10122171-0128160 B	2.93 ± 0.04	293.0 ± 0.3	1.94 ± 0.01	2.01 ± 0.05	...	165	110	...	1.96	10 <sup>-4</sup>	10 <sup>-2</sup>	yes	1.2 (1.1)	...
10165115+3935281 B	0.28 ± 0.01	104.2 ± 2.4	1.47 ± 0.28	1.26 ± 0.05	...	19	9	...	...	...	...	...	...	...
10280144+3029003 B	0.44 ± 0.02	313.8 ± 2.2	2.9 ± 0.03	2.0 ± 0.13	...	32	7	...	...	...	...	...	25.3	...
10364483+1521394 C	0.87 ± 0.02	228.0 ± 1.3	0.94 ± 0.03	0.71 ± 0.08	...	43	16	...	0.76	...	...	yes <sup>b</sup>	2.4	...
10364483+1521394 B	0.73 ± 0.01	228.6 ± 1.3	1.01 ± 0.01	0.68 ± 0.08	...	41	15	...	0.76	...	...	yes <sup>b</sup>	2.4	...
10473203+3508261 B	3.91 ± 0.02	3.6 ± 0.4	3.71 ± 0.03	2.93 ± 0.05	...	217	104	...	3.83	10 <sup>-3</sup>	10 <sup>-3</sup>	yes	1.1 (1.0)	...



**Table 6**  
(Continued)

Primary 2MASS ID	Separation ( $''$ )	P. A. ( $^\circ$ )	Robo-AO			Detection S/N			Gaia DR2			Phys. assoc.	RUWE prim. (comp)	HIP-Gaia prim. $\chi^2_{\text{acc}}$
			$i'$	$J$	$H$	$i'$	$J$	$H$	$\Delta m_G$	$\Delta \pi / \pi$	$\Delta \mu / \mu$			
10590395+6349283 B	1.57 ± 0.01	324.7 ± 0.4	2.29 ± 0.03	1.31 ± 0.09	...	81	53	...	2.0	10 <sup>-3</sup>	0.1	yes	1.4 (2.0)	...
11055616+3534446 B	0.42 ± 0.01	108.2 ± 1.8	3.51 ± 0.03	3.05 ± 0.09	...	11	5	...	...	...	...	...	5.8	...
11101383+3114033 B	0.87 ± 0.04	229.2 ± 3.2	2.26 ± 0.17	1.92 ± 0.34	...	65	24	...	...	...	...	...	2.3	...
11102968+0432586 B	0.78 ± 0.01	257.1 ± 0.7	...	1.71 ± 0.05	...	...	28	...	...	...	...	...	6.0	...
11165318+3251037 B	0.77 ± 0.02	269.9 ± 2.6	0.97 ± 0.08	1.57 ± 0.08	...	56	26	...	0.58	...	...	...	...	...
11240434+3808108 B	8.03 ± 0.04	129.1 ± 0.3	4.7 ± 0.1	2.83 ± 0.08	...	64	65	...	4.26	10 <sup>-4</sup>	10 <sup>-2</sup>	yes	1.3 (0.9)	...
11281625+3136017 B	1.06 ± 0.03	146.2 ± 0.9	1.55 ± 0.18	1.01 ± 0.08	...	160	47	...	1.32	...	...	...	3.2	...
11372461+4727445 B	1.15 ± 0.01	144.1 ± 0.6	1.04 ± 0.03	0.45 ± 0.08	...	99	50	...	0.31	10 <sup>-2</sup>	0.2	yes	1.3 (1.8)	421.1
11385010+3342182 B	0.88 ± 0.02	271.7 ± 1.8	2.65 ± 0.13	2.79 ± 0.08	...	41	10	...	...	...	...	...	2.5	...
11435638-2906027 <sup>(SC)</sup> B	2.59 ± 0.03	91.4 ± 0.7	0.26 ± 0.01	...	0.28 ± 0.1	354	...	135	0.34	10 <sup>-3</sup>	10 <sup>-2</sup>	yes	1.2 (1.2)	...
11471895+3818232 B	1.52 ± 0.01	346.5 ± 0.6	0.36 ± 0.02	0.58 ± 0.08	...	236	55	...	0.27	10 <sup>-2</sup>	10 <sup>-2</sup>	yes	3.4 (2.1)	...
11560817-0409325 B	3.76 ± 0.01	190.1 ± 0.4	0.36 ± 0.01	0.23 ± 0.05	...	193	149	...	0.4	10 <sup>-3</sup>	10 <sup>-2</sup>	yes	1.7 (1.3)	1.2
12015580+3357366 B	4.09 ± 0.02	151.1 ± 0.4	3.75 ± 0.11	3.33 ± 0.15	...	84	30	...	3.82	0.1	0.1	yes	3.3 (1.1)	...
12082885+1327090 B	1.81 ± 0.02	323.9 ± 0.5	2.17 ± 0.01	1.71 ± 0.05	...	211	83	...	2.15	10 <sup>-3</sup>	0.2	yes	1.3 (2.4)	...
12115308+1249135 B	1.17 ± 0.03	179.5 ± 1.3	0.22 ± 0.06	...	0.21 ± 0.29	265	...	81	0.13	10 <sup>-2</sup>	0.1	yes	1.5 (1.9)	...
12215986+2928244 B	0.24 ± 0.01	21.5 ± 4.4	1.4 ± 0.09	1.52 ± 0.14	...	17	7	...	...	...	...	...	...	...
12263225+3347198 B	0.18 ± 0.02	315.6 ± 11.3	...	2.11 ± 0.28	...	...	7	...	...	...	...	...	...	...
12452735+2643454 B	4.78 ± 0.04	5.9 ± 0.3	1.79 ± 0.02	1.37 ± 0.07	...	462	158	...	1.9	10 <sup>-3</sup>	10 <sup>-2</sup>	yes	1.1 (1.1)	...
13061537+2043444 B	1.65 ± 0.02	195.4 ± 0.6	1.91 ± 0.02	1.21 ± 0.07	...	265	87	...	2.04	10 <sup>-3</sup>	0.3	yes	0.9 (2.3)	1386.0
13134536+2218321 B	0.54 ± 0.01	46.8 ± 1.1	...	1.31 ± 0.05	...	...	15	...	...	...	...	...	...	...
13233535+2153068 B	3.25 ± 0.03	190.0 ± 0.7	2.26 ± 0.03	2.03 ± 0.08	...	330	84	...	2.38	10 <sup>-2</sup>	10 <sup>-2</sup>	yes	3.1 (1.5)	...
13402529+2144361 B	0.42 ± 0.03	152.8 ± 1.7	3.76 ± 0.08	2.89 ± 0.1	...	8	4	...	...	...	...	...	4.2	...
13414631+5815197 B	0.85 ± 0.03	252.8 ± 1.1	1.64 ± 0.05	1.32 ± 0.09	...	117	29	...	...	...	...	yes <sup>b</sup>	18.4	...
13474241+2127374 B	1.28 ± 0.02	151.2 ± 1.1	2.1 ± 0.17	1.36 ± 0.16	...	229	55	...	2.88	10 <sup>-3</sup>	10 <sup>-3</sup>	yes <sup>c</sup>	1.2 (1.2)	423.6
13482808+2839154 B	1.93 ± 0.02	288.8 ± 0.4	1.4 ± 0.01	...	1.21 ± 0.09	266	...	176	1.48	10 <sup>-3</sup>	10 <sup>-2</sup>	yes	1.6 (1.6)	...
13482808+2839154 B	1.94 ± 0.02	288.0 ± 0.4	1.4 ± 0.01	1.2 ± 0.05	...	266	93	...	1.48	10 <sup>-3</sup>	10 <sup>-2</sup>	yes	1.6 (1.6)	...
13535682+2422223 B	6.11 ± 0.02	185.5 ± 0.3	1.08 ± 0.01	2.45 ± 0.08	...	396	49	...	1.11	10 <sup>-2</sup>	10 <sup>-2</sup>	yes	3.1 (1.1)	...
14192958+0254365 B	0.5 ± 0.02	337.3 ± 1.4	...	3.05 ± 0.08	...	...	7	...	...	...	...	...	1.2	...
14434861+1817357 B	1.07 ± 0.03	78.2 ± 0.9	0.56 ± 0.15	0.43 ± 0.08	...	169	49	...	0.42	10 <sup>-3</sup>	10 <sup>-3</sup>	yes <sup>c</sup>	1.7 (0.9)	...
14471354+5701550 B	0.48 ± 0.01	53.2 ± 1.6	0.82 ± 0.14	0.65 ± 0.07	...	78	22	...	...	...	...	...	...	...
14514825+1257590 B	0.29 ± 0.02	301.7 ± 2.9	2.1 ± 0.03	1.51 ± 0.05	...	36	11	...	...	...	...	...	...	...
15042411+2620539 B	1.1 ± 0.02	359.2 ± 0.8	1.46 ± 0.03	0.94 ± 0.08	...	168	44	...	1.45	...	...	...	3.8	...
15074262+1946429 B	0.76 ± 0.01	266.7 ± 1.1	0.69 ± 0.15	1.53 ± 0.09	...	116	10	...	0.58	...	...	...	...	...
15471513+0149218 B	0.23 ± 0.01	303.5 ± 4.5	...	1.76 ± 0.06	...	...	8	...	...	...	...	...	4.2	...
15472254+2503372 B	4.14 ± 0.05	326.0 ± 1.5	5.02 ± 0.31	3.54 ± 0.05	...	81	38	...	4.59	1.0	0.8	no	1.4 (1.5)	...
15522029-1347260 <sup>(SC)</sup> B	8.01 ± 0.11	216.2 ± 0.5	...	...	2.63 ± 0.18	...	...	81	5.07	0.8	0.4	no	1.2 (1.1)	...
15542498+2902363 B	8.37 ± 0.02	152.0 ± 0.2	1.61 ± 0.02	1.21 ± 0.07	...	590	182	...	1.67	10 <sup>-3</sup>	10 <sup>-3</sup>	yes	1.1 (1.1)	...
15553178+3512028 B	1.63 ± 0.02	246.7 ± 1.5	2.06 ± 0.03	2.19 ± 0.14	...	200	56	...	2.07	10 <sup>-3</sup>	0.1	yes	1.2 (7.5)	...
15553957+4025135 B	2.36 ± 0.04	117.5 ± 0.9	2.88 ± 0.01	2.36 ± 0.05	...	142	56	...	2.8	10 <sup>-3</sup>	10 <sup>-2</sup>	yes	1.2 (1.2)	...
15553957+4025135 B	2.3 ± 0.02	115.2 ± 0.7	2.88 ± 0.01	...	2.35 ± 0.11	142	...	194	2.8	10 <sup>-3</sup>	10 <sup>-2</sup>	yes	1.2 (1.2)	...
15594729+4403595 B	5.5 ± 0.04	282.6 ± 0.3	6.5 ± 0.03	4.53 ± 0.06	...	67	109	...	6.39	0.1	10 <sup>-2</sup>	yes	7.6 (1.3)	...
16220894+2831402 B	0.46 ± 0.03	78.1 ± 3.2	1.17 ± 0.32	1.23 ± 0.35	...	67	19	...	...	...	...	...	...	...
16245914-1923591 <sup>(SC)</sup> B	4.36 ± 0.02	78.6 ± 0.2	4.7 ± 0.03	...	5.57 ± 0.54	36	...	60	6.43	0.7	1.0	no	1.1 (1.1)	...
16281325-2050253 <sup>(SC)</sup> B	4.46 ± 0.02	199.8 ± 0.2	2.91 ± 0.03	...	1.78 ± 0.09	79	...	143	2.91	0.2	10 <sup>-3</sup>	yes	0.9 (2.9)	...
16284906+3412367 B	1.25 ± 0.01	198.6 ± 0.8	1.25 ± 0.01	0.97 ± 0.05	...	201	63	...	1.34	0.1	0.1	yes	10.4 (1.6)	...

**Table 6**  
(Continued)

Primary 2MASS ID	Separation ( $''$ )	P. A. ( $^\circ$ )	Robo-AO			Detection S/N			Gaia DR2			Phys. assoc.	RUWE prim. (comp)	HIP-Gaia prim. $\chi^2_{\text{acc}}$	
			$i'$	$J$	$H$	$i'$	$J$	$H$	$\Delta m_G$	$\Delta \pi / \pi$	$\Delta \mu / \mu$				
16304072–2018186 <sup>a</sup> (SC) B	3.75 ± 0.07	165.4 ± 1.1	...	...	5.8 ± 0.41	...	...	2	5.56	0.2	10 <sup>-3</sup>	yes	4.4 (1.0)	...	
16304072–2018186 <sup>(SC)</sup> C	4.07 ± 0.11	283.6 ± 1.6	...	...	3.08 ± 0.17	...	...	50	4.16	0.9	0.9	no	4.4 (1.5)	...	
16350111+3130290 B	3.14 ± 0.08	316.3 ± 0.4	4.37 ± 0.01	3.44 ± 0.05	...	...	...	46	32	...	...	no	1.3 (1.0)	...	
16393042–1939470 <sup>(SC)</sup> B	0.37 ± 0.01	234.2 ± 2.9	3.53 ± 0.09	...	2.32 ± 0.17	20	...	13	...	...	...	...	9.2	...	
16590962+2058160 B	0.6 ± 0.02	122.6 ± 1.7	1.31 ± 0.14	...	0.81 ± 0.15	134	...	39	1.03	10 <sup>-3</sup>	0.2	yes <sup>c</sup>	3.3 (2.2)	...	
17035283+3211456 B	1.42 ± 0.01	153.4 ± 0.5	2.12 ± 0.01	1.6 ± 0.05	...	...	...	221	65	...	1.91	10 <sup>-2</sup>	yes	10.1 (11.0)	...
17035283+3211456 B	1.41 ± 0.02	154.6 ± 0.6	2.12 ± 0.01	...	1.42 ± 0.15	221	...	74	1.91	10 <sup>-2</sup>	0.2	yes	10.1 (11.0)	...	
17082102+1949492 B	7.74 ± 0.04	114.0 ± 0.2	3.94 ± 0.04	...	5.67 ± 0.44	174	...	19	3.68	1.0	0.9	no	1.1 (1.0)	...	
17245426+5026327 B	9.0 ± 0.03	198.0 ± 0.2	1.17 ± 0.0	1.2 ± 0.05	...	603	135	...	1.2	10 <sup>-3</sup>	10 <sup>-2</sup>	yes	1.2 (1.1)	...	
17374869+2257163 B	4.27 ± 0.02	188.5 ± 0.3	0.18 ± 0.0	0.13 ± 0.08	...	427	125	...	0.21	10 <sup>-4</sup>	10 <sup>-2</sup>	yes	1.0 (1.1)	9.1	
18295024+4032276 B	2.82 ± 0.02	326.1 ± 0.6	4.75 ± 0.05	...	4.01 ± 0.35	71	...	64	4.33	1.0	0.9	no	1.0 (1.1)	...	
18361922+1336261 C	4.52 ± 0.07	40.5 ± 1.3	5.83 ± 0.02	7.67 ± 1.05	...	27	2	...	-0.76	1.0	1.0	no <sup>c</sup>	1.2(1.0)	...	
18361922+1336261 B	4.42 ± 0.04	316.0 ± 0.8	3.33 ± 0.0	4.08 ± 0.23	...	410	113	...	-0.16	1.0	1.0	no <sup>c</sup>	1.2 (1.3)	...	
19074283+3232396 B	0.33 ± 0.01	260.5 ± 2.4	1.82 ± 0.04	2.33 ± 0.05	...	36	8	...	...	...	...	yes <sup>b</sup>	...	...	
19185703+4951305 B	6.67 ± 0.03	134.8 ± 0.2	2.75 ± 0.09	1.43 ± 0.07	...	526	157	...	3.13	10 <sup>-2</sup>	0.3	yes	0.9 (49.5)	2.6	
19205158+1903362 B	0.55 ± 0.01	197.1 ± 1.5	1.78 ± 0.28	1.0 ± 0.05	...	64	20	...	...	...	...	...	...	...	
19501592+3146598 B	0.64 ± 0.03	39.6 ± 1.8	1.26 ± 0.19	0.73 ± 0.12	...	105	27	...	...	...	...	...	9.5	...	
19501592+3146598 C	7.73 ± 0.03	267.4 ± 0.2	5.1 ± 0.31	5.76 ± 0.17	...	86	15	...	5.55	1.0	1.0	no	9.5 (1.0)	...	
19535443+4424541 B	0.41 ± 0.01	183.3 ± 1.4	3.18 ± 0.03	1.77 ± 0.1	...	23	11	...	...	...	...	yes <sup>b</sup>	10.5	...	
19535443+4424541 C	5.87 ± 0.02	68.2 ± 0.3	0.5 ± 0.02	0.37 ± 0.07	...	520	145	...	0.45	10 <sup>-3</sup>	10 <sup>-3</sup>	yes	10.5 (1.2)	...	
20231789+6710096 B	1.08 ± 0.03	224.3 ± 1.9	1.19 ± 0.07	0.74 ± 0.08	...	134	33	...	0.41	10 <sup>-3</sup>	0.1	yes	3.1 (3.7)	...	
20301067+2650344 C	9.74 ± 0.01	317.9 ± 0.2	3.8 ± 0.0	3.93 ± 0.08	...	384	45	...	3.5	1.0	0.9	no	24.0	11.3	
20301067+2650344 B	0.56 ± 0.02	225.3 ± 1.1	0.74 ± 0.04	1.17 ± 0.08	...	82	16	...	...	...	...	yes <sup>b</sup>	24.0	11.3	
20512890+3104224 B	1.4 ± 0.01	134.4 ± 0.7	1.21 ± 0.08	0.75 ± 0.08	...	267	72	...	1.24	10 <sup>-3</sup>	10 <sup>-2</sup>	yes	1.5 (2.6)	...	
20512890+3104224 C	4.54 ± 0.02	22.3 ± 0.2	4.13 ± 0.01	4.96 ± 0.08	...	183	21	...	3.62	1.0	1.0	no	1.5 (1.2)	...	
21095739+0321217 B	2.58 ± 0.02	181.6 ± 0.4	1.88 ± 0.0	...	1.39 ± 0.1	406	...	145	1.91	10 <sup>-3</sup>	10 <sup>-2</sup>	yes	1.2 (1.2)	...	
22173212+3319453 B	1.24 ± 0.03	157.5 ± 2.0	0.97 ± 0.03	0.43 ± 0.14	...	108	54	...	0.95	10 <sup>-3</sup>	10 <sup>-2</sup>	yes	1.3 (7.1)	...	
23074095+0803597 B	0.25 ± 0.09	110.8 ± 20.2	...	...	2.06 ± 0.35	...	...	10	...	...	...	...	1.1	...	
23103988+7020144 B	0.81 ± 0.14	39.4 ± 7.1	...	2.33 ± 0.13	...	...	18	...	...	...	...	...	1.2	...	
23264139-1504313 B	1.15 ± 0.02	289.1 ± 0.7	...	1.35 ± 0.08	...	...	31	...	0.64	...	...	...	2.6	...	
23350028+0136193 B	0.85 ± 0.01	346.9 ± 1.7	...	1.49 ± 0.17	...	...	19	...	2.44	...	...	yes <sup>b</sup>	1.0	211.5	
23350028+0136193 C	1.22 ± 0.01	354.0 ± 1.4	...	1.22 ± 0.18	...	...	25	...	2.44	...	...	yes <sup>b</sup>	1.0	211.5	
23450868+3003184 B	0.4 ± 0.02	99.7 ± 2.2	1.69 ± 0.02	1.47 ± 0.47	...	63	16	...	...	...	...	...	...	...	
23533563+1206167 B	5.8 ± 0.02	164.9 ± 0.2	0.78 ± 0.0	0.29 ± 0.05	...	494	149	...	0.85	10 <sup>-3</sup>	10 <sup>-3</sup>	yes	1.0 (1.4)	1.0	

**Notes.** (SC) Sco-Cen member.

<sup>a</sup> Although 2MASS 16304072–2018186 has a detection significance below our threshold, we have confirmed that it is real from PanSTARRS observations and a match in Gaia DR2.

<sup>b</sup> 2MASS J02514973+2929131 and 2MASS J13414631+5815197: Cortés-Contreras et al. (2017); 2MASS J10364483+1521394: Calissendorff et al. (2017); 2MASS J19535443+4424541: Tokovinin (2017); 2MASS J20301067+2650344: Malkov et al. (2012); 2MASS J19074283+3232396 and 2MASS J23350028+0136193: Mann et al. (2019).

<sup>c</sup> From Gaia EDR3 astrometry.

(A machine-readable version of the table is available.)

**Table 7**  
Binary Companion Properties: Physically Associated

2MASS ID	Separation (au)	$i'$	Apparent Magnitude			Absolute Magnitude			vis-IR color		Mass <sup>a</sup> ( $M_{\text{Jup}}$ )
			$J$	$H$	$i'$	$J$	$H$	$i'-J$	$i'-H$		
00024011+3821453 B	58.52 ± 1.45	11.99 ± 0.04	...	9.34 ± 0.1	8.91 ± 0.04	...	6.26 ± 0.35	...	2.65 ± 0.11	175–495	
00175864+2057192 B	259.33 ± 0.74	10.05 ± 0.0	8.99 ± 0.13	...	7.83 ± 0.0	6.77 ± 0.13	...	1.06 ± 0.13	...	172–504	
00213183+1934253 B	233.75 ± 1.5	14.18 ± 0.02	...	11.18 ± 0.1	10.77 ± 0.02	...	7.77 ± 0.14	...	3.0 ± 0.1	64–247	
00233382+0947356 B	141.53 ± 0.55	...	9.89 ± 0.05	...	...	6.92 ± 0.07	...	>4.53	...	154–477	
01563544+1228047 B	133.42 ± 1.1	11.18 ± 0.01	9.26 ± 0.08	...	7.86 ± 0.01	5.93 ± 0.09	...	1.92 ± 0.08	...	>312	
01584363+3515281 B	83.16 ± 0.69	...	9.85 ± 0.07	...	...	6.58 ± 0.11	...	>4.88	...	195–535	
02022823+1034533 B	13.46 ± 0.31	11.12 ± 0.07	...	8.21 ± 0.15	10.31 ± 0.07	...	7.39 ± 0.26	...	2.91 ± 0.16	83–303	
02170213+2719305 B	120.22 ± 0.88	10.38 ± 0.01	9.95 ± 0.07	...	6.54 ± 0.01	6.11 ± 0.09	...	0.43 ± 0.07	...	275–614	
02514973+2929131 B	20.92 ± 0.99	11.55 ± 0.21	10.1 ± 0.14	...	9.7 ± 0.21	8.25 ± 0.25	...	1.45 ± 0.26	...	61–249	
04310001+3647548 B	28.52 ± 0.6	12.36 ± 0.03	10.41 ± 0.08	...	9.56 ± 0.03	7.61 ± 0.25	...	1.95 ± 0.09	...	96–357	
04504680+2353317 B	59.83 ± 1.27	12.02 ± 0.51	10.77 ± 0.25	...	7.8 ± 0.51	6.55 ± 0.33	...	1.25 ± 0.57	...	201–541	
04540567+2200545 B	290.98 ± 3.11	13.41 ± 0.03	12.69 ± 0.08	...	9.06 ± 0.03	8.33 ± 0.28	...	0.73 ± 0.09	...	57–238	
05015881+0958587 B	34.24 ± 0.4	10.22 ± 0.03	...	7.26 ± 0.11	8.34 ± 0.03	...	5.38 ± 0.14	...	2.96 ± 0.12	>313	
06575703+6219197 B	13.48 ± 0.14	...	9.75 ± 0.07	...	...	9.45 ± 0.07	...	...	...	20–128	
09011748+1515523 B	92.99 ± 0.83	8.4 ± 0.01	7.04 ± 0.05	...	7.08 ± 0.01	5.71 ± 0.05	...	1.36 ± 0.05	...	>363	
09124007+2647327 B	231.34 ± 1.34	15.59 ± 0.03	12.13 ± 0.05	...	11.73 ± 0.03	8.28 ± 0.14	...	3.45 ± 0.06	...	60–245	
09261352+3728253 B	327.82 ± 3.11	13.86 ± 0.0	11.82 ± 0.08	...	8.36 ± 0.0	6.31 ± 0.27	...	2.05 ± 0.08	...	239–582	
10122171-0128160 B	116.62 ± 1.69	13.54 ± 0.01	11.53 ± 0.05	...	10.54 ± 0.01	8.53 ± 0.08	...	2.0 ± 0.05	...	49–212	
10473203+3508261 B	392.93 ± 4.78	16.19 ± 0.03	13.64 ± 0.05	...	11.18 ± 0.03	8.63 ± 0.36	...	2.55 ± 0.06	...	45–201	
10590395+6349283 B	157.23 ± 1.29	14.69 ± 0.03	11.86 ± 0.09	...	9.69 ± 0.03	6.86 ± 0.18	...	2.83 ± 0.09	...	161–488	
11240434+3808108 B	148.31 ± 0.96	17.24 ± 0.1	12.75 ± 0.08	...	15.91 ± 0.1	11.42 ± 0.1	...	4.49 ± 0.13	...	13–51	
11372461+4727445 B	39.41 ± 0.53	10.32 ± 0.03	7.86 ± 0.08	...	7.65 ± 0.03	5.19 ± 0.14	...	2.46 ± 0.09	...	>511	
11435638-2906027 <sup>(SC)</sup> B	233.38 ± 3.22	12.61 ± 0.01	...	10.38 ± 0.1	7.83 ± 0.01	...	5.6 ± 0.17	...	2.23 ± 0.1	309–332	
11471895+3818232 B	129.53 ± 1.43	12.6 ± 0.02	10.95 ± 0.08	...	7.96 ± 0.02	6.3 ± 0.2	...	1.65 ± 0.08	...	240–582	
11560817-0409325 B	182.91 ± 0.8	10.48 ± 0.01	9.38 ± 0.05	...	7.05 ± 0.01	5.94 ± 0.07	...	1.1 ± 0.05	...	>310	
12015580+3357366 B	605.37 ± 11.28	16.53 ± 0.11	14.32 ± 0.15	...	10.68 ± 0.11	8.47 ± 0.73	...	2.22 ± 0.19	...	52–220	
12082885+1327090 B	68.33 ± 0.8	15.28 ± 0.01	12.23 ± 0.05	...	12.4 ± 0.01	9.35 ± 0.15	...	3.04 ± 0.05	...	21–135	
12115308+1249135 B	72.7 ± 2.08	11.39 ± 0.06	...	9.04 ± 0.29	7.42 ± 0.06	...	5.08 ± 0.33	...	2.35 ± 0.3	>380	
12452735+2643454 B	283.88 ± 2.37	13.69 ± 0.02	11.48 ± 0.07	...	9.82 ± 0.02	7.61 ± 0.12	...	2.21 ± 0.07	...	96–356	
13061537+2043444 B	32.52 ± 0.41	10.31 ± 0.02	8.03 ± 0.07	...	8.84 ± 0.02	6.56 ± 0.08	...	2.28 ± 0.07	...	199–539	
13233535+2153068 B	233.92 ± 2.54	13.8 ± 0.03	12.07 ± 0.08	...	9.52 ± 0.03	7.79 ± 0.18	...	1.73 ± 0.08	...	85–322	
13414631+5815197 B	16.94 ± 0.59	12.47 ± 0.05	10.05 ± 0.09	...	10.98 ± 0.05	8.56 ± 0.22	...	2.42 ± 0.1	...	48–208	
13474241+2127374 B	38.4 ± 0.49	11.96 ± 0.17	9.58 ± 0.16	...	9.58 ± 0.17	7.2 ± 0.16	...	2.38 ± 0.23	...	127–431	
13482808+2839154 B	222.06 ± 3.21	14.8 ± 0.01	...	12.12 ± 0.09	9.5 ± 0.01	...	6.81 ± 0.31	...	2.69 ± 0.09	120–405	
13482808+2839154 B	222.92 ± 2.81	14.8 ± 0.01	12.57 ± 0.05	...	9.5 ± 0.01	7.27 ± 0.3	...	2.23 ± 0.05	...	121–419	
13535682+2422223 B	330.46 ± 1.35	13.92 ± 0.01	13.18 ± 0.08	...	10.26 ± 0.01	9.52 ± 0.11	...	0.74 ± 0.08	...	20–123	
14434861+1817357 B	95.05 ± 2.36	12.73 ± 0.15	10.86 ± 0.08	...	7.98 ± 0.15	6.1 ± 0.08	...	1.87 ± 0.17	...	277–615	
15542498+2902363 B	446.73 ± 1.32	14.43 ± 0.02	11.91 ± 0.07	...	10.79 ± 0.02	8.27 ± 0.08	...	2.52 ± 0.08	...	60–246	
15553178+3512028 B	45.16 ± 0.63	14.55 ± 0.03	11.11 ± 0.14	...	12.34 ± 0.03	8.9 ± 0.15	...	3.44 ± 0.14	...	26–173	
15553957+4025135 B	349.62 ± 6.68	15.77 ± 0.01	13.43 ± 0.05	...	9.91 ± 0.01	7.58 ± 0.33	...	2.33 ± 0.05	...	97–362	
15553957+4025135 B	341.39 ± 4.0	15.77 ± 0.01	...	12.81 ± 0.11	9.91 ± 0.01	...	6.96 ± 0.35	...	2.95 ± 0.12	109–380	
15594729+4403595 B	234.42 ± 2.02	16.93 ± 0.03	13.04 ± 0.06	...	13.79 ± 0.03	9.89 ± 0.11	...	3.89 ± 0.06	...	18–99	
16281325-2050253 <sup>(SC)</sup> B	1101.23 ± 66.35	15.75 ± 0.03	...	12.36 ± 0.09	8.79 ± 0.03	...	5.4 ± 3.11	...	3.39 ± 0.1	359–377	
16284906+3412367 B	196.65 ± 2.87	14.55 ± 0.01	12.19 ± 0.05	...	8.57 ± 0.01	6.2 ± 0.43	...	2.36 ± 0.05	...	258–600	
16304072–2018186 <sup>(SC)</sup> B	551.63 ± 26.99	...	...	16.07 ± 0.41	...	...	10.23 ± 1.83	...	>0.4	12–15	
16590962+2058160 B	10.77 ± 0.34	11.85 ± 0.14	...	8.55 ± 0.15	10.59 ± 0.14	...	7.3 ± 0.2	...	3.29 ± 0.21	88–318	
17035283+3211456 B	26.52 ± 0.36	12.17 ± 0.01	9.49 ± 0.05	...	10.81 ± 0.01	8.12 ± 0.14	...	2.69 ± 0.05	...	67–267	

**Table 7**  
(Continued)

2MASS ID	Separation (au)	$i'$	Apparent Magnitude			Absolute Magnitude			vis-IR color		Mass <sup>a</sup> ( $M_{\text{Jup}}$ )
			$J$	$H$	$i'$	$J$	$H$	$i'-J$	$i'-H$		
17035283+3211456 B	26.34 ± 0.41	12.17 ± 0.01	...	8.72 ± 0.15	10.81 ± 0.01	...	7.36 ± 0.2	...	3.45 ± 0.15	85–308	
17245426+5026327 B	422.72 ± 1.54	12.4 ± 0.0	10.96 ± 0.05	...	9.04 ± 0.0	7.6 ± 0.05	...	1.44 ± 0.05	...	96–357	
17374869+2257163 B	97.32 ± 0.38	8.58 ± 0.0	7.22 ± 0.08	...	6.79 ± 0.0	5.42 ± 0.08	...	1.37 ± 0.08	...	>439	
19074283+3232396 B	2.78 ± 0.09	10.48 ± 0.04	9.57 ± 0.05	...	10.88 ± 0.04	9.97 ± 0.05	...	0.91 ± 0.07	...	17–94	
19185703+4951305 B	427.07 ± 24.47	13.63 ± 0.09	10.89 ± 0.07	...	9.6 ± 0.09	6.86 ± 1.51	...	2.74 ± 0.12	...	161–488	
20231789+6710096 B	23.68 ± 0.65	13.73 ± 0.07	10.82 ± 0.08	...	12.02 ± 0.07	9.11 ± 0.09	...	2.91 ± 0.11	...	23–155	
20301067+2650344 B	11.36 ± 0.4	9.51 ± 0.04	8.3 ± 0.08	...	7.97 ± 0.04	6.76 ± 0.29	...	1.21 ± 0.09	...	173–506	
20512890+3104224 B	82.15 ± 0.89	11.18 ± 0.08	9.96 ± 0.08	...	7.34 ± 0.08	6.12 ± 0.14	...	1.22 ± 0.11	...	273–613	
21095739+0321217 B	116.57 ± 0.87	13.53 ± 0.0	...	10.01 ± 0.1	10.26 ± 0.0	...	6.73 ± 0.12	...	3.52 ± 0.1	127–419	
22173212+3319453 B	116.27 ± 3.03	11.6 ± 0.03	10.26 ± 0.14	...	6.74 ± 0.03	5.4 ± 0.48	...	1.35 ± 0.14	...	>448	
23533563+1206167 B	215.42 ± 0.97	11.11 ± 0.0	8.96 ± 0.05	...	8.26 ± 0.0	6.11 ± 0.07	...	2.15 ± 0.05	...	276–615	

**Notes.** (SC) Sco-Cen member.

<sup>a</sup> Estimated mass ranges are from evolutionary isochrone models (Chabrier et al. 2000; Baraffe et al. 2015) calculated for ages 10–200 Myr, except Sco-Cen members were calculated for 5–15 Myr.

(A machine-readable version of the table is available.)

**Table 8**  
Binary Companion Candidate Properties: Physical Association to Be Confirmed

2MASS ID	Separation (au)	Apparent Magnitude			Absolute Magnitude			vis-IR color		Mass <sup>a</sup> ( $M_{\text{Jup}}$ )	$P(N_{\text{background}} \geq 1)$ (%)
		$i'$	$J$	$H$	$i'$	$J$	$H$	$i'-J$	$i'-H$		
00360847+4530575 B	11.03 ± 0.37	...	9.82 ± 0.08	...	...	8.18 ± 0.08	...	...	...	64–259	4.88 ± 0.11
01564996+4142303 B	5.92 ± 0.9	13.25 ± 0.2	11.94 ± 0.1	...	...	10.82 ± 0.2	9.52 ± 0.12	...	1.3 ± 0.22	20–123	3.97 ± 0.1
02154870+2458501 B	33.64 ± 0.84	12.56 ± 0.03	...	9.61 ± 0.19	9.12 ± 0.03	...	...	6.16 ± 0.23	...	186–510	1.13 ± 0.04
02284694+1538535 B	25.76 ± 0.86	12.23 ± 0.03	...	9.14 ± 0.14	9.51 ± 0.03	...	...	6.42 ± 0.16	...	157–469	0.96 ± 0.03
02405251+4452365 B	8.72 ± 0.38	11.68 ± 0.07	10.89 ± 0.51	...	...	9.95 ± 0.07	9.16 ± 0.55	...	0.79 ± 0.51	23–150	5.41 ± 0.11
02453008+2620233 B	11.55 ± 1.0	12.84 ± 0.23	11.04 ± 0.15	...	...	8.78 ± 0.23	6.99 ± 1.28	...	1.79 ± 0.28	147–466	2.01 ± 0.07
03051963+2131219 B	22.81 ± 0.77	13.42 ± 0.08	10.71 ± 0.31	...	...	10.73 ± 0.08	8.02 ± 0.43	...	2.71 ± 0.32	73–284	1.74 ± 0.06
03051963+2131219 B	23.03 ± 0.6	12.67 ± 0.1	...	9.49 ± 0.15	9.97 ± 0.1	...	...	6.8 ± 0.34	...	122–407	1.24 ± 0.04
03072749+5018081 B	25.08 ± 0.69	13.28 ± 0.03	11.38 ± 0.14	...	...	9.89 ± 0.03	7.99 ± 0.14	...	1.9 ± 0.15	74–288	13.45 ± 0.16
03093085+4543586 B	8.97 ± 0.35	10.97 ± 0.14	8.41 ± 0.38	...	...	9.75 ± 0.14	7.2 ± 0.43	...	2.56 ± 0.4	127–431	11.14 ± 0.15
05354082+6047451 B	24.45 ± 1.04	...	11.41 ± 0.2	...	...	...	8.52 ± 0.33	...	...	50–213	4.82 ± 0.11
06114391+4813113 B	11.65 ± 0.81	...	11.94 ± 0.05	...	...	...	8.72 ± 0.93	...	>1.97	42–191	5.19 ± 0.11
06584690+2843004 B	36.98 ± 1.47	...	...	12.81 ± 0.13	...	...	...	9.71 ± 0.63	...	17–86	3.45 ± 0.06
07110918+1312442 B	13.59 ± 1.04	13.29 ± 0.08	11.17 ± 0.05	...	...	10.02 ± 0.08	7.9 ± 0.88	...	2.12 ± 0.1	79–303	6.69 ± 0.12
08551482+4242427 B	72.85 ± 3.92	15.52 ± 0.02	13.16 ± 0.08	...	...	10.11 ± 0.02	7.76 ± 1.76	...	2.35 ± 0.08	87–328	1.18 ± 0.05
09021527+3007590 B	108.48 ± 3.21	13.77 ± 0.25	11.77 ± 0.05	...	...	8.33 ± 0.25	6.33 ± 0.05	...	2.01 ± 0.25	236–578	2.49 ± 0.08
09200048+3052397 B	15.25 ± 0.55	11.07 ± 0.23	9.3 ± 0.08	...	...	8.3 ± 0.23	6.53 ± 0.08	...	1.77 ± 0.25	203–544	1.59 ± 0.06
09354051+3831339 B	45.35 ± 1.56	13.93 ± 0.2	11.96 ± 0.05	...	...	9.41 ± 0.2	7.43 ± 0.05	...	1.97 ± 0.2	107–389	1.0 ± 0.05
10013178+3841174 B	21.35 ± 1.08	15.2 ± 0.03	14.1 ± 0.08	...	...	10.73 ± 0.03	9.63 ± 0.81	...	1.1 ± 0.09	19–115	0.98 ± 0.05
10165115+3935281 B	16.09 ± 0.67	12.52 ± 0.28	10.55 ± 0.05	...	...	8.73 ± 0.28	6.76 ± 0.05	...	1.97 ± 0.28	173–505	0.83 ± 0.05
10280144+3029003 B	31.2 ± 1.97	14.19 ± 0.03	11.42 ± 0.13	...	...	9.93 ± 0.03	7.16 ± 1.43	...	2.77 ± 0.13	130–437	0.85 ± 0.05
11055616+3534446 B	47.51 ± 1.9	16.41 ± 0.03	14.02 ± 0.09	...	...	11.16 ± 0.03	8.77 ± 0.77	...	2.39 ± 0.1	37–186	0.88 ± 0.05
11101383+3114033 B	93.33 ± 4.31	14.94 ± 0.17	12.9 ± 0.34	...	...	9.79 ± 0.17	7.75 ± 0.44	...	2.04 ± 0.38	87–330	0.84 ± 0.05
11102968+0432586 B	72.56 ± 2.25	...	12.35 ± 0.05	...	...	...	7.51 ± 0.9	...	...	101–374	1.43 ± 0.06
11165318+3251037 B	78.87 ± 1.92	13.45 ± 0.08	12.29 ± 0.08	...	...	8.4 ± 0.08	7.23 ± 0.08	...	1.17 ± 0.11	124–424	0.76 ± 0.04
11281625+3136017 B	32.48 ± 1.01	13.52 ± 0.18	10.78 ± 0.08	...	...	11.08 ± 0.18	8.34 ± 0.18	...	2.74 ± 0.19	57–237	0.82 ± 0.04
11385010+3342182 B	111.76 ± 3.05	15.38 ± 0.13	13.56 ± 0.08	...	...	9.86 ± 0.13	8.05 ± 0.51	...	1.81 ± 0.16	71–279	0.75 ± 0.04
12215986+2928244 B	32.11 ± 1.67	14.71 ± 0.09	12.95 ± 0.14	...	...	9.12 ± 0.09	7.35 ± 0.14	...	1.76 ± 0.17	113–403	0.74 ± 0.04
12263225+3347198 B	10.23 ± 0.96	...	11.71 ± 0.28	...	...	...	7.98 ± 0.28	...	>0.86	74–290	0.74 ± 0.04
13134536+2218321 B	36.16 ± 0.73	...	11.31 ± 0.05	...	...	...	7.18 ± 0.05	...	>4.14	128–433	0.8 ± 0.04
13402529+2144361 B	85.88 ± 5.58	16.54 ± 0.08	14.34 ± 0.1	...	...	10.01 ± 0.08	7.81 ± 1.27	...	2.2 ± 0.13	84–319	0.85 ± 0.05
14192958+0254365 B	10.35 ± 0.37	...	13.01 ± 0.08	...	...	...	11.41 ± 0.09	...	>3.6	13–51	1.26 ± 0.06
14471354+5701550 B	15.45 ± 0.4	11.92 ± 0.14	10.57 ± 0.07	...	...	9.38 ± 0.14	8.02 ± 0.07	...	1.36 ± 0.16	72–283	1.12 ± 0.05
14514825+1257590 B	23.84 ± 1.57	14.86 ± 0.03	11.99 ± 0.05	...	...	10.3 ± 0.03	7.44 ± 0.05	...	2.86 ± 0.06	107–387	1.65 ± 0.06
15042411+2620539 B	84.61 ± 1.35	13.83 ± 0.03	11.49 ± 0.08	...	...	9.4 ± 0.03	7.06 ± 0.22	...	2.34 ± 0.09	140–455	1.26 ± 0.06
15074262+1946429 B	47.15 ± 0.89	14.24 ± 0.15	12.55 ± 0.09	...	...	10.27 ± 0.15	8.58 ± 0.09	...	1.69 ± 0.18	47–206	1.29 ± 0.06
15471513+0149218 B	4.32 ± 0.21	...	12.4 ± 0.06	...	...	...	11.08 ± 0.12	...	>5.2	14–56	3.05 ± 0.09
16220894+2831402 B	31.26 ± 1.85	13.46 ± 0.32	11.35 ± 0.35	...	...	9.31 ± 0.32	7.2 ± 0.35	...	2.11 ± 0.48	127–430	2.58 ± 0.08
16393042-1939470 <sup>(SC)</sup> B	65.9 ± 3.68	16.94 ± 0.09	...	13.43 ± 0.17	10.67 ± 0.09	...	...	7.16 ± 1.83	...	60–119	5.96 ± 0.08
19205158+1903362 B	23.69 ± 0.53	12.49 ± 0.28	10.71 ± 0.05	...	...	9.33 ± 0.28	7.55 ± 0.05	...	1.78 ± 0.28	99–367	43.22 ± 0.21
19501592+3146598 B	21.38 ± 0.94	11.6 ± 0.19	9.91 ± 0.12	...	...	8.99 ± 0.19	7.3 ± 0.33	...	1.69 ± 0.22	118–413	43.94 ± 0.21
23074095+0803597 B	12.03 ± 4.13	...	...	10.97 ± 0.35	...	...	...	7.55 ± 0.35	...	75–278	3.02 ± 0.06
23103988+7020144 B	36.27 ± 6.4	...	11.86 ± 0.13	...	...	...	8.6 ± 0.14	...	>2.78	46–204	9.82 ± 0.14
23264139-1504313 B	32.15 ± 0.55	...	11.34 ± 0.08	...	...	...	9.1 ± 0.16	...	...	23–156	1.04 ± 0.05
23450868+3003184 B	13.68 ± 0.51	12.64 ± 0.02	11.3 ± 0.47	...	...	9.99 ± 0.02	8.66 ± 0.47	...	1.33 ± 0.48	44–198	2.21 ± 0.07

**Notes.** (SC) Sco-Cen member.

<sup>a</sup> Estimated mass ranges are from evolutionary isochrone models (Chabrier et al. 2000; Baraffe et al. 2015) calculated for ages 10–200 Myr, except for Sco-Cen members, which were calculated for 5–15 Myr.

(A machine-readable version of the table is available.)

**Table 9**  
Triple Companion Candidate Properties

2MASS ID	Separation (au)	Apparent Magnitude			Absolute Magnitude			vis-IR color		Mass <sup>a</sup> ( $M_{\text{Jup}}$ )	Phys. assoc.	$P(N_{\text{background}} \geq 1)$ (%)
		$i'$	$J$	$H$	$i'$	$J$	$H$	$i'-J$	$i'-H$			
05242572+1922070 B	$113.22 \pm 1.32$	$13.49 \pm 0.37$	$11.67 \pm 0.09$	...	$9.62 \pm 0.37$	$7.81 \pm 0.21$	...	$1.82 \pm 0.38$	...	84–319	yes	$7.95 \pm 0.13$
05242572+1922070 C	$20.92 \pm 0.75$	...	$11.34 \pm 0.29$	...	...	$7.51 \pm 0.52$	...	>3.58	...	102–375	...	...
10364483+1521394 B	$17.22 \pm 0.31$	$11.98 \pm 0.03$	$9.46 \pm 0.08$	...	$10.5 \pm 0.03$	$7.98 \pm 0.09$	...	$2.52 \pm 0.08$	...	74–290	yes	...
10364483+1521394 C	$14.47 \pm 0.28$	$12.05 \pm 0.01$	$9.43 \pm 0.08$	...	$10.57 \pm 0.01$	$7.95 \pm 0.09$	...	$2.62 \pm 0.08$	...	76–295	yes	...
19535443+4424541 B	$1.93 \pm 0.05$	$12.03 \pm 0.03$	$9.56 \pm 0.1$	...	$13.67 \pm 0.03$	$11.2 \pm 0.1$	...	$2.47 \pm 0.11$	...	13–54	yes	...
19535443+4424541 C	$27.38 \pm 0.11$	$9.35 \pm 0.02$	$8.16 \pm 0.07$	...	$11.01 \pm 0.02$	$9.82 \pm 0.07$	...	$1.19 \pm 0.07$	...	18–103	yes	...
23350028+0136193 B	$17.69 \pm 0.26$	...	$8.38 \pm 0.17$	...	...	$6.78 \pm 0.17$	...	>3.48	...	170–501	yes	...
23350028+0136193 C	$25.38 \pm 0.28$	...	$8.1 \pm 0.18$	...	...	$6.51 \pm 0.18$	...	>3.8	...	205–547	yes	...

**Notes.** (SC) Sco-Cen member.

<sup>a</sup> Estimated mass ranges are from evolutionary isochrone models (Chabrier et al. 2000; Baraffe et al. 2015) calculated for ages 10–200 Myr, except for Sco-Cen members, which were calculated for 5–15 Myr.

(A machine-readable version of the table is available.)

**Table 10**  
Companion Candidates Found in Catalogs

Primary 2MASS ID	Catalog	Obs Date (UT)	Separation ( $''$ )	P. A. ( $^{\circ}$ )	Mass $M_{\odot}$	SpT
01584363+3515281 B	This Work	2017 Oct 29	$1.85 \pm 0.01$	$86.3 \pm 0.3$	...	...
	WDS	2015	1.9	271	...	...
02022823+1034533 <sup>a</sup> C	This Work	2019 Oct 16	$3.99 \pm 0.02$	$185.9 \pm 0.3$	...	...
	WDS	2014	4.7	191	...	...
02170213+2719305 B	This Work	2017 Oct 28	$2.05 \pm 0.01$	$183.6 \pm 0.4$	...	...
	WDS	2015	2.1	183	...	...
02284694+1538535 B	This Work	2019 Oct 16	$0.73 \pm 0.02$	$137.9 \pm 1.2$	...	...
	B19	2014 Nov 7	$0.84 \pm 0.04$	$147 \pm 3$	...	...
02514973+2929131 B	This Work	2017 Oct 29	$0.89 \pm 0.04$	$243.6 \pm 5.0$	...	...
	C17	2011 Oct 24	$0.63 \pm 0.01$	$249.4 \pm 1.3$	$M_B$ 0.15	M5
	WDS	2016	0.8	246	...	M4V+M5V
03093085+4543586 B	This Work	2017 Oct 30	$0.51 \pm 0.02$	$20.2 \pm 3.0$	...	...
	L20	2016 Feb 16	$0.35 \pm 0.07$	$23.9 \pm 8.0$	$M_B/M_A$ 0.7	...
	WDS	2011	0.2	182	...	M2V+M4
05015881+0958587 B	This Work	2019 Oct 17	$1.45 \pm 0.01$	$141.9 \pm 0.7$	...	...
	C17	2014 Feb 28	$1.35 \pm 0.01$	$148.9 \pm 0.3$	$M_B$ 0.33	...
	WDS	2018	1.4	145	...	M3V:
06575703+6219197 B	This Work	2017 Nov 6	$1.17 \pm 0.01$	$248.1 \pm 0.6$	...	...
	WDS	2015	1.3	246	...	M4.5
06584690+2843004 B	This Work	2019 Oct 17	$0.89 \pm 0.02$	$275.5 \pm 1.7$	...	...
	B19	2014 Mar 25	$1.08 \pm 0.06$	$247 \pm 3$	...	...
09124007+2647327 B	This Work	2017 Nov 3	$3.92 \pm 0.01$	$183.5 \pm 0.2$	...	...
	WDS	2015	4.0	185	...	...
09200048+3052397 B	This Work	2018 Apr 9	$0.43 \pm 0.02$	$71.3 \pm 1.6$	...	...
	B19	2014 Mar 25	$0.42 \pm 0.03$	$66 \pm 3$	...	...
10122171-0128160 B	This Work	2018 May 10	$2.93 \pm 0.04$	$293.0 \pm 0.3$	...	...
	WDS	2015	3.0	293	...	M3+M5
10364483+1521394 C	This Work	2018 May 6	$0.87 \pm 0.02$	$228.0 \pm 1.3$	...	...
	WDS AB	2009	1.0	160	...	M3.5+M4.5
10364483+1521394 B	This Work	2018 May 6	$0.73 \pm 0.01$	$228.6 \pm 1.3$	...	...
	WDS AB	2009	1.0	160	...	M3.5+M4.5
10590395+6349283 B	This Work	2018 May 10	$1.57 \pm 0.01$	$324.7 \pm 0.4$	...	...
	WDS	2015	1.5	324	...	...
11240434+3808108 B	This Work	2018 Apr 12	$8.03 \pm 0.04$	$129.1 \pm 0.3$	...	...
	WDS	2015	8.2	131	...	M8V+M4.5V
11281625+3136017 B	This Work	2018 Apr 8	$1.06 \pm 0.03$	$146.2 \pm 0.9$	...	...
	WDS	2015	1.1	145	...	M3+M4
11372461+4727445 B	This Work	2017 Jun 12	$1.15 \pm 0.01$	$144.1 \pm 0.6$	...	...
	WDS	2010	1.1	129	...	K4V
11435638-2906027 <sup>(SC)</sup> B	This Work	2019 May 29	$2.59 \pm 0.03$	$91.4 \pm 0.7$	...	...
	WDS	2015	2.7	94	...	...
11560817-0409325 B	This Work	2018 May 10	$3.76 \pm 0.01$	$190.1 \pm 0.4$	...	...
	WDS	2015	3.8	192	...	M0V
12115308+1249135 B	This Work	2019 May 26	$1.17 \pm 0.03$	$179.5 \pm 1.3$	...	...
	B19	2015 Mar 8	$1.17 \pm 0.02$	$3 \pm 2$	...	...
12452735+2643454 B	This Work	2018 Apr 10	$4.78 \pm 0.04$	$5.9 \pm 0.3$	...	...
	WDS	2015	4.7	6	...	...
13061537+2043444 B	This Work	2018 May 31	$1.65 \pm 0.02$	$195.4 \pm 0.6$	...	...
	B19	2015 Jun 8	$1.61 \pm 0.03$	$197 \pm 3$	...	...
	WDS	2015	1.6	199	...	K4V
13134536+2218321 B	This Work	2018 Apr 11	$0.54 \pm 0.01$	$46.8 \pm 1.1$	...	...
	L20	2016 Mar 17	$0.52 \pm 0.07$	$43.5 \pm 5.0$	...	...
13414631+5815197 B	This Work	2018 May 8	$0.85 \pm 0.03$	$252.8 \pm 1.1$	...	...
	C17	2014 Mar 2	$0.68 \pm 0.02$	$251.3 \pm 1.4$	$M_B$ 0.21	M4
	WDS	2015	0.7	251	...	M3+M4
13474241+2127374 B	This Work	2018 Apr 11	$1.28 \pm 0.02$	$151.2 \pm 1.1$	...	...
	B19	2015 Jun 7	$1.33 \pm 0.04$	$150 \pm 3$	...	...
	WDS	2016	1.3	151	...	M0
15553178+3512028 B	This Work	2018 Apr 6	$1.63 \pm 0.02$	$246.7 \pm 1.5$	...	...
	L20	2016 Mar 11	$1.57 \pm 0.07$	$251.3 \pm 2.0$	$M_B/M_A$ 0.46	...
	B19	2014 Mar 25	$1.64 \pm 0.04$	$252 \pm 1$	...	...
	WDS	2015	1.6	253	...	M4+M7
15594729+4403595 B	This Work	2018 Apr 16	$5.5 \pm 0.04$	$282.6 \pm 0.3$	...	...

**Table 10**  
(Continued)

Primary 2MASS ID	Catalog	Obs Date (UT)	Separation ( $''$ )	P. A. ( $^{\circ}$ )	Mass $M_{\odot}$	SpT
	WDS	2015	5.6	284	...	M1e+M8
16590962+2058160 B	This Work	2019 May 29	$0.6 \pm 0.02$	$122.6 \pm 1.7$	...	...
	WDS	2009	0.7	139	...	M3+M4
17035283+3211456 B	This Work	2018 Apr 8	$1.42 \pm 0.01$	$153.4 \pm 0.5$	...	...
	This Work	2019 May 22	$1.41 \pm 0.02$	$154.6 \pm 0.6$	...	...
	L20	2016 Mar 17	$1.42 \pm 0.07$	$152.2 \pm 1.0$	...	...
	B19	2015 Mar 8	$1.44 \pm 0.03$	$150 \pm 1$	...	...
	WDS	2009	1.3	143	...	M2+M4
19205158+1903362 B	This Work	2017 Jun 14	$0.55 \pm 0.01$	$197.1 \pm 1.5$	...	...
	B19	2015 Jun 10	$0.51 \pm 0.04$	$196 \pm 1$	...	...
19501592+3146598 B	This Work	2017 Oct 30	$0.64 \pm 0.03$	$39.6 \pm 1.8$	...	...
	L20	2016 Jul 29	$0.59 \pm 0.07$	$45.3 \pm 5.0$	$M_B/M_A$ 0.69	...
19535443+4424541 B	This Work	2017 Oct 30	$0.41 \pm 0.01$	$183.3 \pm 1.4$	...	...
	WDS Aa Ab	2012	0.6	350	...	M5.5V+M7V
20231789+6710096 B	This Work	2018 May 6	$1.08 \pm 0.03$	$224.3 \pm 1.9$	...	...
	WDS	2015	1.2	225	...	M5+M5
20301067+2650344 B	This Work	2017 Jun 14	$0.56 \pm 0.02$	$225.3 \pm 1.1$	...	...
	L20	2016 Jun 27	$0.56 \pm 0.07$	$227.9 \pm 5.0$	$M_B/M_A$ 0.88	...
	WDS AB	2016	0.6	230	...	M1V
20512890+3104224 B	This Work	2017 Jun 14	$1.4 \pm 0.01$	$134.4 \pm 0.7$	...	...
	L20	2016 Jul 26	$1.42 \pm 0.07$	$134.9 \pm 1.0$	$M_B/M_A$ 0.8	...
	WDS	2015	1.4	134	...	...
23350028+0136193 <sup>b</sup> B	This Work	2017 Nov 2	$0.85 \pm 0.01$	$346.9 \pm 1.7$	...	...
	WDS BC	2018	0.3	196	...	...
23350028+0136193 <sup>b</sup> C	This Work	2017 Nov 2	$1.22 \pm 0.01$	$354.0 \pm 1.4$	...	...
	WDS BC	2018	0.3	196	...	...

**Notes.** (SC) Sco-Cen member. L20: Lamman et al. (2020); C17: Cortés-Contreras et al. (2017); B19: Bowler et al. (2019); WDS: Washington Double Star catalog.

<sup>a</sup> We determined this companion candidate to be a background object from Gaia DR2 measurements (See Table 6).

<sup>b</sup> The WDS lists the separation and PA of the BC components of the system while we list the separation and PA for AB and AC.









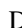

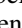


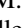
**Table 11**  
All Observed Targets

2MASS ID	R.A. J2000	Decl. J2000	$m_J$ (mag)	Obs. Date (UT)	Seeing ( $''$ )	Reduction Pipeline	Filter(s)	IR Contrast Limits ( $\Delta m$ ) [0 $''$ 5, 1 $''$ 0, 2 $''$ 0, 3 $''$ 0]	Max Sep. (au)	Comp. Candidate?
00004701+1624101	00:00:47.01	+16:24:10.1	9.32	2017 Nov 6	2.01	All frames	$i', J$	1.4, 3.8, 4.9, 5.8	391	...
00024011+3821453	00:02:40.12	+38:21:45.31	9.71	2019 Oct 12	1.24	All frames	$i', H$	3.5, 4.8, 5.0, 7.9	244	Y
00082730+1725274	00:08:27.3	+17:25:27.49	7.81	2019 Oct 13	...	All frames	$i', H$	2.7, 3.9, 6.2, 8.0	128	...
00175864+2057192	00:17:58.64	+20:57:19.2	8.69	2017 Oct 30	1.38	All frames	$i', J$	1.5, 4.4, 6.4, 7.7	228	Y
00205719+1738160	00:20:57.19	+17:38:16.08	8.37	2019 Oct 16	1.01	90% GenSTAC	$i', H$	2.8, 3.0, 4.4, 5.9	176	...

**Note.** (SC) Sco-Cen member.

(This table is available in its entirety as supporting data in the online version of this article.)

## ORCID iDs

Maïssa Salama  <https://orcid.org/0000-0002-5082-6332>  
 James Ou  <https://orcid.org/0000-0002-8439-7767>  
 Christoph Baranec  <https://orcid.org/0000-0002-1917-9157>  
 Michael C. Liu  <https://orcid.org/0000-0003-2232-7664>  
 Brendan P. Bowler  <https://orcid.org/0000-0003-2649-2288>  
 Mark Chun  <https://orcid.org/0000-0002-8462-0703>  
 Dmitry A. Duvvuri  <https://orcid.org/0000-0001-5060-8733>  
 Sean Goebel  <https://orcid.org/0000-0003-3763-2418>  
 Rebecca Jensen-Clem  <https://orcid.org/0000-0003-0054-2953>  
 Nicholas M. Law  <https://orcid.org/0000-0001-9380-6457>  
 Reed Riddle  <https://orcid.org/0000-0002-0387-370X>  
 Zhoujian Zhang  <https://orcid.org/0000-0002-3726-4881>

## References

- Allers, K. N., & Liu, M. C. 2013, *ApJ*, **772**, 79  
 Atkinson, D., Hall, D., Jacobson, S., & Baker, I. M. 2018, *AJ*, **155**, 220  
 Atkinson, D. E., Hall, D. N. B., Jacobson, S. M., & Baker, I. M. 2017, *AJ*, **154**, 265  
 Bai, Y., Liu, J., Wicker, J., et al. 2018, *ApJS*, **235**, 16  
 Baraffe, I., Homeier, D., Allard, F., & Chabrier, G. 2015, *A&A*, **577**, A42  
 Baranec, C., Atkinson, D., Riddle, R., et al. 2015, *ApJ*, **809**, 70  
 Baranec, C., Riddle, R., Law, N. M., et al. 2014, *ApJL*, **790**, L8  
 Baron, F., Lafrenière, D., Artigau, É., et al. 2019, *AJ*, **158**, 187  
 Barrado y Navascués, D., Stauffer, J. R., & Jayawardhana, R. 2004, *ApJ*, **614**, 386  
 Bate, M. R., Bonnell, I. A., & Bromm, V. 2003, *MNRAS*, **339**, 577  
 Best, W. M. J., Magnier, E. A., Liu, M. C., et al. 2018, *ApJS*, **234**, 1  
 Bochanski, J. J., Hawley, S. L., Covey, K. R., et al. 2010, *AJ*, **139**, 2679  
 Bonavita, M. 2020, Exo-DMC: Exoplanet Detection Map Calculator, v1.1b, [ascl:2010.008](https://arxiv.org/abs/2010.008)  
 Bonavita, M., Chauvin, G., Desidera, S., et al. 2012, *A&A*, **537**, A67  
 Bond, C. Z., Cetre, S., Lilley, S., et al. 2020, *JATIS*, **6**, 039003  
 Bowler, B. P. 2016, *PASP*, **128**, 102001  
 Bowler, B. P., Blunt, S. C., & Nielsen, E. L. 2020, *AJ*, **159**, 63  
 Bowler, B. P., Hinkley, S., Ziegler, C., et al. 2019, *ApJ*, **877**, 60  
 Bowler, B. P., Liu, M. C., Shkolnik, E. L., & Tamura, M. 2015a, *ApJS*, **216**, 7  
 Bowler, B. P., & Nielsen, E. L. 2018, in Occurrence Rates from Direct Imaging Surveys, ed. H. J. Deeg & J. A. Belmonte (Cham: Springer), 155  
 Bowler, B. P., Shkolnik, E. L., Liu, M. C., et al. 2015b, *ApJ*, **806**, 62  
 Brandt, T. D. 2018, *ApJS*, **239**, 31  
 Brandt, T. D., Dupuy, T. J., & Bowler, B. P. 2019, *AJ*, **158**, 140  
 Burgasser, A. J., Kirkpatrick, J. D., Reid, I. N., et al. 2003, *ApJ*, **586**, 512  
 Calissendorff, P., Janson, M., Köhler, R., et al. 2017, *A&A*, **604**, A82  
 Chabrier, G., Baraffe, I., Allard, F., & Hauschildt, P. 2000, *ApJ*, **542**, 464  
 Chabrier, G., Hennebelle, P., & Charlot, S. 2014, *ApJ*, **796**, 75  
 Close, L. M., Siegler, N., Freed, M., & Biller, B. 2003, *ApJ*, **587**, 407  
 Cortés-Contreras, M., Béjar, V. J. S., Caballero, J. A., et al. 2017, *A&A*, **597**, A47  
 Cushing, M. C., Vacca, W. D., & Rayner, J. T. 2004, *PASP*, **116**, 362  
 de Zeeuw, P. T., Hoogerwerf, R., de Bruijne, J. H. J., Brown, A. G. A., & Blaauw, A. 1999, *AJ*, **117**, 354  
 Deacon, N. R., Liu, M. C., Magnier, E. A., et al. 2014, *ApJ*, **792**, 119  
 Duchêne, G., & Kraus, A. 2013, *ARA&A*, **51**, 269  
 Dupuy, T. J., Allen, P. R., Kraus, A. L., et al. 2013, *AN*, **334**, 36  
 Durisen, R. H., Boss, A. P., Mayer, L., et al. 2007, Protostars and Planets VI (Tucson, AZ: Univ. Arizona Press), 607  
 Faherty, J. K., Bochanski, J. J., Gagné, J., et al. 2018, *ApJ*, **863**, 91  
 Finger, G., Baker, I., Alvarez, D., et al. 2014, *Proc. SPIE*, **9148**, 914817  
 Frith, J., Pinfield, D. J., Jones, H. R. A., et al. 2013, *MNRAS*, **435**, 2161  
 Fruchter, A. S., & Hook, R. N. 2002, *PASP*, **114**, 144  
 Gaia Collaboration, Brown, A. G. A., Vallenari, A., et al. 2018, *A&A*, **616**, A1  
 Gaia Collaboration, Prusti, T., de Bruijne, J. H. J., et al. 2016, *A&A*, **595**, A1  
 Goebel, S. B., Hall, D. N. B., Guyon, O., Warmbier, E., & Jacobson, S. M. 2018, *JATIS*, **4**, 026001  
 Haakonsen, C. B., & Rutledge, R. E. 2009, *ApJS*, **184**, 138  
 Hippler, S., Brandner, W., Scheithauer, S., et al. 2020, *Instruments*, **4**, 20  
 Hirsch, L. A., Ciardi, D. R., Howard, A. W., et al. 2017, *AJ*, **153**, 117  
 Horch, E. P., Casetti-Dinescu, D. I., Camarata, M. A., et al. 2017, *AJ*, **153**, 212  
 Horch, E. P., Howell, S. B., Everett, M. E., & Ciardi, D. R. 2014, *ApJ*, **795**, 60  
 Howard, W. S., Law, N. M., Ziegler, C. A., Baranec, C., & Riddle, R. 2018, *AJ*, **155**, 59  
 Janson, M., Hormuth, F., Bergfors, C., et al. 2012, *ApJ*, **754**, 44  
 Jensen-Clem, R., Duvvuri, D. A., Riddle, R., et al. 2018, *AJ*, **155**, 32  
 Jiménez-Esteban, F. M., Solano, E., & Rodrigo, C. 2019, *AJ*, **157**, 78  
 Kammerer, J., Ireland, M. J., Martinache, F., & Girard, J. H. 2019, *MNRAS*, **486**, 639  
 Kastner, J., Chalfour, M., Binks, A., et al. 2018, in 20th Cambridge Workshop on Cool Stars, Stellar Systems and the Sun, ed. S. Wolk (Boston, MA: Harvard Univ. Press), 90  
 Kirkpatrick, J. D., Looper, D. L., Burgasser, A. J., et al. 2010, *ApJS*, **190**, 100  
 Kratter, K., & Lodato, G. 2016, *ARA&A*, **54**, 271  
 Kraus, A. L., Herczeg, G. J., Rizzuto, A. C., et al. 2017, *ApJ*, **838**, 150  
 Kraus, A. L., & Hillenbrand, L. A. 2007, *AJ*, **134**, 2340  
 Lambrechts, M., & Johansen, A. 2012, *A&A*, **544**, A32  
 Lamman, C., Baranec, C., Berta-Thompson, Z. K., et al. 2020, *AJ*, **159**, 139  
 Lannier, J., Delorme, P., Lagrange, A. M., et al. 2016, *A&A*, **596**, A83  
 Larson, R. B. 2002, *MNRAS*, **332**, 155  
 Law, N. M. 2006, PhD thesis, Institute of Astronomy & Selwyn College, Cambridge Univ.  
 Law, N. M., Hodgkin, S. T., & Mackay, C. D. 2008, *MNRAS*, **384**, 150  
 Lawrence, A., Warren, S. J., Almaini, O., et al. 2007, *MNRAS*, **379**, 1599  
 Li, J. Z., & Hu, J. Y. 1998, *A&AS*, **132**, 173  
 Liu, M. C., Dupuy, T. J., & Allers, K. N. 2016, *ApJ*, **833**, 96  
 Malkov, O. Y., Tamazian, V. S., Docobo, J. A., & Chulkov, D. A. 2012, *A&A*, **546**, A69  
 Mann, A. W., Dupuy, T., Kraus, A. L., et al. 2019, *ApJ*, **871**, 63  
 Martin, D. C., Fanson, J., Schiminovich, D., et al. 2005, *ApJL*, **619**, L1  
 Mason, B. D., Wycoff, G. L., Hartkopf, W. I., Douglass, G. G., & Worley, C. E. 2001, *AJ*, **122**, 3466  
 Morrissey, P., Conrow, T., Barlow, T. A., et al. 2007, *ApJS*, **173**, 682  
 Muirhead, P. S., Dressing, C. D., Mann, A. W., et al. 2018, *AJ*, **155**, 180  
 Naud, M.-E., Artigau, É., & Doyon, R. 2017, *AJ*, **154**, 129  
 Newton, E. R., Charbonneau, D., Irwin, J., et al. 2014, *AJ*, **147**, 20  
 Pourbaix, D., Tokovinin, A. A., Batten, A. H., et al. 2004, *A&A*, **424**, 727  
 Reipurth, B., Clarke, C. J., Boss, A. P., et al. 2014, in Protostars and Planets VI, ed. H. Beuther et al. (Tucson, AZ: Univ. Arizona Press), 267  
 Reipurth, B., & Mikkola, S. 2012, *Natur*, **492**, 221  
 Riddle, R. L., Hogstrom, K., Papadopoulos, A., Baranec, C., & Law, N. M. 2014, *Proc. SPIE*, **9152**, 91521E  
 Rodriguez, D. R., Zuckerman, B., Kastner, J. H., et al. 2013, *ApJ*, **774**, 101  
 Rodríguez Martínez, R., Lopez, L. A., Shappee, B. J., et al. 2020, *ApJ*, **892**, 144  
 Salama, M., Baranec, C., Jensen-Clem, R., et al. 2016, *Proc. SPIE*, **9909**, 99091A  
 Salama, M., Ou, J., Baranec, C., et al. 2018, *Proc. SPIE*, **10703**, 1070307  
 Schlaufman, K. C. 2018, *ApJ*, **853**, 37  
 Skrutskie, M. F., Cutri, R. M., Stiening, R., et al. 2006, *AJ*, **131**, 1163  
 Tokovinin, A. 2017, *ApJ*, **844**, 103  
 Veras, D., Crepp, J. R., & Ford, E. B. 2009, *ApJ*, **696**, 1600  
 Villa Vélez, J. A., Brown, A. G. A., & Kenworthy, M. A. 2018, *RNAAS*, **2**, 58  
 Winters, J. G., Henry, T. J., Jao, W.-C., et al. 2019, *AJ*, **157**, 216  
 Wright, E. L., Eisenhardt, P. R. M., Mainzer, A. K., et al. 2010, *AJ*, **140**, 1868  
 Wright, N. J., & Mamajek, E. E. 2018, *MNRAS*, **476**, 381  
 Zhang, Z., Liu, M. C., Best, W. M. J., et al. 2018, *ApJ*, **858**, 41